Structure Formation in Supraparticles Composed of Spherical and Elongated Particles

Melis Yetkin[1+], Yashraj M. Wani[2+], Kritika Kritika[2,3,4], Michael P. Howard[5], Michael Kappl[1], Hans-Jürgen Butt[1*], Arash Nikoubashman[2,3,4*]

[1]Department of Physics at Interfaces, Max-Planck Institute for Polymer Research, Ackermannweg 10, 55128 Mainz, Germany
[2]Institute of Physics, Johannes Gutenberg University of Mainz, Staudingerweg 7, 55128 Mainz, Germany
[3]Leibniz-Institut für Polymerforschung Dresden e.V., Hohe Straße 6, 01069 Dresden, Germany
[4]Institut für Theoretische Physik, Technische Universität Dresden, 01069 Dresden, Germany
[5]Department of Chemical Engineering, Auburn University, Auburn, Alabama 36849, USA
+These authors contributed equally to this work.

* Corresponding authors: butt@mpip-mainz.mpg.de & anikouba@ipfdd.de

ABSTRACT

We studied the evaporation-induced formation of supraparticles from dispersions of elongated colloidal particles using experiments and computer simulations. Aqueous droplets containing a dispersion of ellipsoidal and spherical polystyrene particles were dried on superamphiphobic surfaces at different humidity that lead to varying evaporation rates. Supraparticles made from only ellipsoidal particles showed short-range lateral ordering at the supraparticle surface and random orientations in the interior, regardless of the evaporation rate. Particle-based simulations corroborated the experimental observations in the evaporation-limited regime ($Pe \gg 1$) and showed an increase in the local nematic ordering as the diffusion-limited regime ($Pe \leq 1$) was reached. A thin shell of ellipsoids was observed at the surface when supraparticles were made from binary mixtures of ellipsoids and spheres. Image analysis revealed that the supraparticle porosity increased with increasing aspect ratio of the ellipsoids.

INTRODUCTION

Colloidal particles can assemble into supraparticles of various sizes, architectures, and compositions.[1,2] The material properties of supraparticles can be engineered through the choice of the colloidal "building blocks" as well as their composition and arrangement within the supraparticle. Multiple types of materials, ranging from nanometer-sized quantum dots[3] or metal organic frameworks[4] to micrometer-sized polystyrene (PS) particles,[5] with different shape and chemistry can be used as building blocks to create supraparticles. The supraparticles may have emergent properties that surpass the mere sum of their parts, arising from the interactions between different types of building blocks.[1,2] Therefore, supraparticles are versatile materials with potential applications in many fields of science and technology, including catalysis,[1,6–8] gas adsorption and sensing,[4,9] drug encapsulation and delivery,[10,11] photonics[12–14] and energy production and storage.[15,16]

Wet self-assembly methods have been commonly used to fabricate supraparticles by forming them inside or around droplet templates, such as emulsion droplets suspended in liquid media.[12,17–20] However, these methods have certain drawbacks, including the need for additional processing liquids that require proper disposal as well as only limited control over the final supraparticle morphology. Dry self-assembly methods offer an alternative approach where supraparticles are obtained by evaporating droplets into air.[1,5,21] These techniques do not need additional processing liquids and simplify the collection of the assembled supraparticles.[21] Commonly used dry self-assembly methods include Leidenfrost levitation[22,23] and spray-drying,[24–29] in which droplets dry in a contact free environment. These methods are typically performed at high temperatures, where evaporation takes only a few seconds. Therefore, studying structure formation with these techniques in real time is difficult and requires complex instruments, such as rotating anode-based X-ray sources or small-angle X-ray scattering.[30,31] Further, the fast evaporation conditions make it quite difficult to control the final supraparticle shape and the distribution of the colloidal particles inside the supraparticle.[32] For levitated droplets, additional parameters such as the thermal conductivity of the substrate can introduce challenges in controlling the resulting supraparticle shapes.[30,32]

Alternatively, supraparticles can be fabricated by evaporating droplets supported on solid substrates. The wetting property of the substrate is important, as it directly determines the deposition characteristics in the contact region. Superamphiphobic surfaces repel water and also nonpolar liquids, surfactants, and protein solutions. Droplets on such surfaces acquire high

contact angles (CA > 150°) and roll off easily (tilting angle < 10°), while the interfacial area between the liquid and solid is extremely small ($\ll V^{2/3}$, where V is the droplet volume).[33–36] Further, superamphiphobic surfaces typically have a highly porous structure, which allows the liquid to evaporate through the substrate, leading to almost radially symmetric evaporation. As a result, the method suppresses contact line pinning and hence the coffee-ring effect,[37–39] as well as temperature-induced Marangoni flow inside the droplet.[40] In contrast to Leidenfrost levitation and spray-drying, evaporation from superamphiphobic surfaces occurs at much longer timescales, which also makes studying the structure formation of supraparticles more convenient.[41]

Conventionally, spherical particles have been used to fabricate supraparticles of various structures and compositions by tuning the particle concentrations and processing parameters such as the evaporation rate.[1,5,11,41–43] Examples include supraparticles having a core-shell morphology of larger (core) and smaller (shell) PS spheres,[5] PLGA/ciprofloxacin supraparticles prepared in solvents of various polarity,[11] multicomponent spherical mesoporous supraparticles of metal oxides such as TiO_2/SnO_2 and TiO_2/ZnO,[42] and supraparticles with non-spherical shape induced by the addition of salt.[41] The shape of the colloidal particles themselves is a powerful but still largely unexplored handle for controlling supraparticle structure.[44–46] Experiments[47] and simulations[48] of bulk systems have shown that rod-like particles tend to pack into more open random structures compared to their spherical counterparts. Simulations of sphere-rod mixtures in the bulk also revealed demixing transitions under the right conditions[49] and decreasing packing with increasing rod aspect ratios.[50] Recently, Jacucci *et al.* fabricated spherical supraparticles from silica nanorods *via* emulsion evaporation, and obtained a core-shell morphology, with a disordered core and an ordered shell.[51] The surface ordering of the nanorods was tuned from smectic to isotropic by adding salt into the dispersion, which resulted in a decrease of reflectance. It was noted that the light scattering efficiency could be further improved upon increasing the range of nanorod ordering.[51] Van der Hoeven *et al.* assembled silica-coated gold nanorod supraparticles to enhance the Raman scattering of analyte molecules. Gold nanorods exhibited superior and highly tunable plasmonic properties compared to spheres due to their longitudinal surface plasmon resonance in the visible and near-infrared spectrum.[52] Wang *et al.* showed that drying droplets containing lanthanide fluoride nanoplatelets could be utilized to fabricate supraparticles with tailored optoelectronic properties.[53]

Although these prior works have hinted at the possibilities of using anisotropic building blocks for creating supraparticles, systematic studies investigating the influence of the aspect ratio of the colloidal particles, mixing colloidal particles with different aspect ratios, and evaporation rate on structure formation are still lacking. To better understand these aspects and to develop design strategies, we performed experiments and simulations on the formation of supraparticles composed of ellipsoidal particles and mixtures of spherical and ellipsoidal particles. In the experiments, we used PS colloidal particles to differentiate the effect of topology from the effect of materials properties. As the density of an aqueous PS dispersion is close to that of water, and ellipsoidal particles- having similar interaction potentials and surface chemistry- can be prepared from PS, we were able to focus on the physics of supraparticle formation. We found that (i) the ordering of the ellipsoids could be tuned by changing the evaporation rate, (ii) ellipsoids tended to form a thin shell with short-range orientational order on the surface,

and (iii) supraparticle porosity tended to increase with increasing ellipsoid aspect ratio due to random packing in the interior.

EXPERIMENTAL METHODS

Materials. Methyl trichlorosilane (TCMS, 99%) and hexadecane (Reagent Plus, 99%) were purchased from Sigma Aldrich. 1H,1H,2H,2H-Perfluorodecyltrichlorosilane (PFDTS, 96%) was purchased from Alfa Aesar. N-Hexane (≥95%), toluene (≥99.8%), acetone (≥99.8%), and isopropyl alcohol (IPA, ≥99.8%) were purchased from Fisher Chemical. Ethanol (≥99.8%) was provided by Honeywell Research Chemicals. Ultrapure water with a resistivity of 18.2 MΩ·cm was obtained using a Sartorius Arium 611 VF water purification system. Glass slides 25 × 75 mm^2 in size were provided by Menzel-Gläser, Germany. PS particles (zeta potential ≈ -56 mV, with –COOH groups on the surface) with a diameter of 408 nm (polydispersity index 0.034) were synthesized by the copolymerization of styrene and acrylic acid using surfactant-free emulsion polymerization.[54] The synthesized particles were purified by several centrifugation cycles and were finally redispersed in ultrapure water. Polyvinyl alcohol (PVA, M_w 115000 g/mol, degree of hydrolysis 86.5 – 89%) was purchased from VWR Chemicals. Anionic surfactant sodium dodecyl sulphate (SDS) was purchased from MP Biomedicals.

Preparation of superamphiphobic surfaces. The silicone nanofilaments-based superamphiphobic surfaces were prepared as described before.[35,55] Glass slides were sonicated in toluene, acetone, and ethanol and dried by nitrogen flow. Then, glass slides were oxygen plasma treated at 30 W for 2 min (Diener Electronic Femto). The activated glass slides were immersed in 360 mL toluene with 166 ppm water content in a Teflon box. The water content of toluene was measured with a Karl Fischer coulometer (Mettler Toledo C20 Compact KF coulometer). 250 µL of TCMS was injected into the Teflon box to initiate the growth of silicone nanofilaments from the glass slides. The chamber was kept sealed for 14 h. After the reaction, the silicone nanofilament-grafted glass slides were rinsed with hexane to remove any unreacted TCMS. To fluorinate the nanofilaments, the grafted glass slides were annealed in a furnace at 200°C for 2 h to obtain a more stable silicone network. Then, the glass slides were again activated with oxygen plasma at 120 W for 2 min and immersed in 120 mL hexane with 0.1 mL PFDTS. After 30 min of reaction, the substrates were rinsed with hexane to remove any unreacted fluorosilanes. The resultant nanofilament-coated glass substrates were homogeneous over a large area [**Fig. S1**].

Preparation of polystyrene ellipsoids. PS ellipsoids were prepared from monodisperse spherical PS particles following the film-stretching method.[56] The preparation procedure is depicted schematically in **Fig. S2**. 5 g of PVA were dissolved in 139 mL distilled water to obtain a 3.5 wt.% aqueous PVA solution. The system was stirred at 375 rpm overnight by keeping the temperature at 80°C. After obtaining a clear PVA solution, about 4 g of 10 wt.% PS particle dispersion was added and stirred at 375 rpm for 5 h to obtain a homogeneous PVA/particle dispersion. The weight ratio of PS to PVA in the final mixture was 0.08. The PVA/particle dispersion was then poured into a flat Teflon mold (15 × 28 cm^2) and was air-dried for 1 day. After evaporation, a particle embedded PVA film was formed. This film was cut into small film strips (3 cm × 8 cm, or, 3 cm × 4 cm, depending on the desired draw ratio). These film strips were stretched in an oven at 140°C. The stretching was done by applying uniaxial tension with a tensile test apparatus (Zwick/Roell Z005 Universal Testing Machine) to the desired length at a speed of 300 mm/min. The films were stretched at draw ratios of 100,

200 and 400% to obtain ellipsoids with varying aspect ratios of about 4, 6, and 11, respectively. The particle size and aspect ratio were calculated by counting 40 particles in a scanning electron microscopy (SEM) image of each batch [**Table 1**]. Several washing steps were required to recover the ellipsoidal particles from the film. After stretching, the PVA/particle film strips were cooled to room temperature while still being clamped in their stretched state and then cut into small pieces (1 cm × 1 cm). The original edges of the stretched films were rejected, as there could be nonuniform stretching near the metal clamps. The small film pieces were soaked in an IPA-water mixture (3:7) (v:v) overnight under magnetic stirring. Then, this mixture was heated to 85°C for 1 h to dissolve the PVA matrix completely. The dispersion was centrifuged at 10000 rpm for 1 h to sediment the particles and the viscous PVA-rich supernatant was decanted. The sediment was dissolved again in an IPA-water mixture (3:7) (v:v) and was centrifuged at 10000 rpm for 1 h. This washing procedure was repeated two times. In the final washing step, the particles were dispersed in water at 90°C under magnetic stirring for 1 h to remove the traces of PVA. Then, the dispersion was centrifuged one last time to recover the PS ellipsoids. The resultant particles were redispersed in an appropriate amount of distilled water depending on the required particle concentration.

Draw ratio (%)	L (μm)	d_e (μm)	$\lambda = L/d_e$
100	0.92±0.05	0.26±0.01	3.5±0.3
200	1.30±0.11	0.21±0.02	6.1±0.8
400	1.95±0.21	0.18±0.02	11±2

Table 1. *The dimensions of the ellipsoids obtained by stretching a film, embedded with 408 nm PS spheres, at different draw ratios. The dimensions (length L and diameter d_e) were determined by analyzing 40 particles each.*

Evaporation of PS dispersion droplets on superamphiphobic surfaces. The aqueous PS dispersions were prepared prior to the evaporation experiments. The volume concentration of PS ellipsoids or spheres in the dispersions was kept around 1%, whereas the total volume concentration of sphere-ellipsoid mixture dispersions was around 0.6% with volume ratio of ellipsoids to spheres 1:1 (v:v). Each system contained 1 mM aqueous SDS solution to stabilize the dispersions. Approximately 1 μL of these dispersions were dispensed onto the superamphiphobic surfaces with the help of an Eppendorf Research Plus pipet, which was equipped with epT.I.P.S. LoRetention Reloads tips. To conduct the evaporation experiments in a controlled manner a humidity chamber was built in-house. The humidity chamber was equipped with an inlet, which allowed nitrogen gas to flow, and a window through which the evaporation process was monitored by a camera (Blackfly S Colour 5.0 MP USB3 Camera). The humidity during evaporation of the dispersion drops was recorded with the help of a humidity sensor inside the chamber. Once the desired humidity was reached, the droplets were dispensed through the holes on top of the chamber, and the holes remained closed throughout the evaporation. The dispersion droplets evaporated at 23°C, either under ambient conditions (relative humidity of 30%) or at a relative humidity of 75%. The supraparticles formed after evaporation were released by slightly inclining the surfaces and were collected in small vials.

Characterization. The morphology of the superamphiphobic surfaces and the supraparticles were imaged by SEM (low voltage LEO 1530 Gemini, Germany). Prior to imaging, the samples were sputter coated with a 7 nm layer of Pt using Safematic Compact Coating Unit-010 to avoid charging. The water concentration in toluene was evaluated using a Karl Fischer coulometer (Mettler Toledo C20 Compact KF coulometer). To detemine the size and polydispersity of the PS particles, dynamic light scattering measurements were carried out on

an ALV spectrometer consisting of a goniometer and an ALV-5004 multiple-tau full-digital correlator (320 channels, angular range from 30° to 150°). A He-Ne Laser (wavelength of 632.8 nm) was used as light source. Measurements were performed at 20°C at 9 angles ranging from 30° to 150°. The zeta potential of the PS particles was measured by a Malvern Zetasizer Nano Z. Using ImageJ software, we performed image analysis with the evaporation videos of the droplets, and recorded the change in droplet volume as a function of time. The volume of the droplets was estimated first by determining an arc through the circumference of the 2D image of one half of the droplet, and then by integrating disc-shaped slices (which are passing through this arc and cutting the central axis of the droplet perpendicularly) around the central axis [**Fig. S3**]. The method assumed no pre-defined droplet shape.

NUMERICAL METHODS

Explicit-solvent simulations of drying colloidal systems are computationally taxing, since they require large numbers of particles and small time steps to capture the fast motion of the solvent particles. As a consequence, such explicit-solvent simulations are typically limited to systems containing a few thousand colloidal particles,[57–59] which is often too small to fully capture structural variations that occur during drying. However, it is often not needed to resolve individual solvent particles, but rather only the solvent's effect on the solute. Therefore, implicit-solvent simulation methods have been used to model drying colloidal systems, and have shown good agreement with experiments in some cases.[60,61] However, at times there are certain qualitative and quantitative discrepancies which are thought to originate from the lack of solvent effects that exist in real systems, such as solvent backflow and hydrodynamic interactions (HI) between the particles.[5,62–64] Therefore, in this study we performed simulations with two methods – (a) Langevin dynamics (LD) [-HI] and (b) multi-particle collision dynamics (MPCD) [+HI].

Langevin dynamics is a widely used implicit solvent technique that incorporates the Stokes friction and Brownian motion of particles in the equations of motion,

$$m\ddot{\mathbf{r}}_i = \boldsymbol{F}_{\mathrm{C}} - \gamma \mathbf{v}_i + \boldsymbol{F}_{\mathrm{R}} \quad (1)$$

where $\boldsymbol{F}_{\mathrm{C}}$ is the force on particle i due to all the conservative interactions in our system, γ is the friction coefficient and $\boldsymbol{F}_{\mathrm{R}}$ is a uniform random force acting on the particle. The magnitude of the random force is chosen in accordance with the fluctuation dissipation theorem, $\langle \boldsymbol{F}_{\mathrm{R}} \rangle = 0$ and $\langle |\boldsymbol{F}_{\mathrm{R}}|^2 \rangle = 6k_{\mathrm{B}}T\gamma/\delta t$. The friction coefficients γ for the different colloidal particles are taken as input parameters which were determined *via* bulk simulations of very dilute ($\phi = 0.0001$) dispersions with MPCD for the elongated and spherical particles.

Multi-particle collision dynamics (MPCD) uses a simplified particle-based solvent model, which undergoes successive free-streaming and stochastic collision steps.[65–67] The solvent is modeled as a set of point particles of number density ρ, having positions $\mathbf{r}_i^{\mathbf{s}}$, velocities $\mathbf{v}_i^{\mathbf{s}}$, and mass m_0. In the free streaming step, solvent particles move ballistically,

$$\mathbf{r}_i^{\mathbf{s}}(t + \Delta t) = \mathbf{r}_i^{\mathbf{s}}(t) + \mathbf{v}_i^{\mathbf{s}}(t)\Delta t \quad (2)$$

where Δt, is the collision timestep, which effectively sets the mean free path of the particles.

The variants of MPCD algorithms differ in their implementation of the collision step. In our study, we use the widely implemented stochastic rotation dynamics (SRD) algorithm,

introduced by Malevanets and Kapral.[65] Particles are first binned into cubic collision cells of length l, where they undergo stochastic rotations as,

$$\mathbf{v}_i^{\mathbf{s}}(t+\Delta t) = \mathbf{u}_c^{\mathbf{s}}(t) + \boldsymbol{\Omega}_c \cdot [\mathbf{v}_i^{\mathbf{s}}(t) - \mathbf{u}_c^{\mathbf{s}}(t)] \qquad (3)$$

where $\mathbf{u}_c^{\mathbf{s}}(t)$ is the average velocity of the particles in a collision cell and $\boldsymbol{\Omega}_c$ is the rotation operator of the cell in which particle i resides at time t. The rotation operator is chosen to have a fixed angle of rotation of 130° around a random axis in each cell. To ensure Galilean invariance, the collision cells are shifted along each direction by a distance uniformly drawn from $[-l/2, l/2]$.[66] A Maxwell-Boltzmann thermostat is applied on the cell level to maintain isothermal conditions. These stochastic collisions build up the HI between the particles. Solute particles are coupled to the solvent through momentum exchange in the collision step, as described further below.

In our MPCD droplet simulations, the solvent can flow through the droplet interface, which likely overpredicts solute entrainment, but still is a significant improvement over complete neglect of hydrodynamic interactions.[68] To minimize unphysical hydrodynamic interactions due to periodic boundary conditions, the simulation box is padded along all directions by the droplet's initial radius.

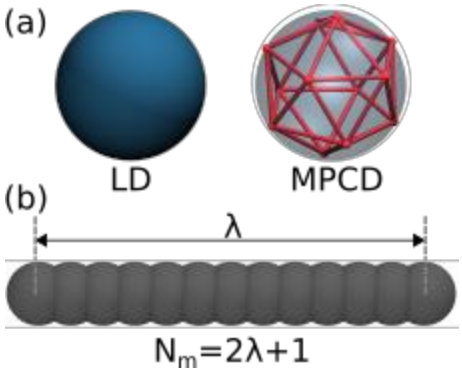

Figure 1. (a) Schematic of spherical particles in LD and MPCD simulations, respectively. The diffuse sphere in MPCD schematic imparts the excluded volume. (b) Schematic of rod-shaped particles in simulations.

Spherical colloidal particles were modelled as nearly hard spheres with diameter $d_s = 3.0l$ *via* the purely repulsive Weeks-Chandler-Andersen (WCA) potential,

$$U_{\mathrm{WCA}}(r) = \begin{cases} 4\epsilon\left[\left(\frac{\sigma}{r-\Delta}\right)^{12} - \left(\frac{\sigma}{r-\Delta}\right)^{6}\right], & r < (r_{\mathrm{cut}} + \Delta) \\ 0, & r \geq (r_{\mathrm{cut}} + \Delta) \end{cases} \qquad (4)$$

where r is the distance between to interacting particles, and we used $\sigma = 1.0l$, $\Delta = 2.0l$, and $r_{\mathrm{cut}} = 2^{1/6}\sigma$. Coupling of the spherical particles to the MPCD solvent requires careful treatment. In this study we used a discrete mesh model to couple the spheres to the solvent.[69,70] In this model, each sphere is represented as a mesh of $N_v = 12$ vertex point particles placed on the surface of the sphere with an additional particle placed in the center of the mesh to impart the nearly hard sphere excluded volume as given above [**Fig. 1(a)**]. The mesh is created using the vertices of an icosahedron that are scaled up such that they lie on the surface of the sphere. The vertex particles are bonded to their nearest neighbors and to the central particle *via* harmonic bonds which ensures that the mesh shape is conserved. The strength of the harmonic bonds was set to, $k_{\mathrm{ico}} = 5000l^{-2}$.

Elongated colloidal particles could, in principle, be described as ellipsoids using anisotropic pair potentials such as the Gay–Berne model; however, it is challenging to couple such a model to the MPCD solvent, given the rather large number of vertex particles needed for covering the ellipsoid surface. Instead, we approximate the ellipsoids of aspect ratio $\lambda = 4,6,11$ using a rod-like ("shish-kebab") model [**Fig. 1(b)**], with every colloidal particle consisting of $N_\mathrm{m} = 2\lambda + 1$ monomers of diameter $d_\mathrm{e} = 1.0l$ bonded *via* a harmonic potential,

$$U_\mathrm{bond}(r) = \frac{1}{2}k_\mathrm{rod}(r - r_0)^2 \qquad (5)$$

with equilibrium length $r_0 = d_\mathrm{e}/2$ and strength $k_\mathrm{rod} = 1000\,\epsilon d_\mathrm{e}^{-2}$. This choice ensured that the excluded volume closely resembled that of a smooth rod. A bending potential between consecutive bond vectors was introduced to make the rods stiff,

$$U_\mathrm{bend}(\theta) = \frac{1}{2}k_\mathrm{bend}(\theta - \theta_0)^2 \qquad (6)$$

with an equilibrium angle, $\theta_0 = \pi$ and strength $k_\mathrm{bend} = 1000\,\epsilon\mathrm{rad}^{-2}$. Such a model for rods in conjunction with MPCD has been studied previously and shown to reproduce the expected diffusion behavior in the bulk.[71] Excluded volume interactions between rods are realized through WCA interactions between the constituent monomers, as described above.

The air-droplet interface in the simulations was modelled using a harmonic potential, located at a distance of R from the center of droplet, acting radially inwards,

$$U(r) = \begin{cases} 0, & r < R \\ \frac{k_\mathrm{drop}}{2}(r - R)^2, & r > R \end{cases} \qquad (7)$$

The interaction strength is analogous to the surface tension of the droplet and was set to $k_\mathrm{drop} = 200\,\varepsilon/{d_\mathrm{e}}^2$. Evaporation of the droplet was simulated by reducing the size of the droplet using the following relation,[64]

$$R^2 = {R_0}^2 - \frac{\alpha}{4\pi}t \qquad (8)$$

where α is the rate of change of surface area which is assumed to be a constant. From the above relation, we can deduce the speed of the receding interface by taking the time derivative,

$$v = \frac{-dR}{dt} = \frac{\alpha}{8\pi R} \qquad (9)$$

Simulation details– MPCD simulations were performed with an initial droplet radius $R_0 = 50d_\mathrm{e}$, whereas LD simulations were performed with droplets of size $R_0 = 50d_\mathrm{e}$ & $100d_\mathrm{e}$. The initial volume fraction of colloidal particles in the droplet was chosen as $\phi_0 = 0.08$ and the droplet was dried until it reached half of its original diameter, corresponding to a final volume fraction of $\phi_\mathrm{f} = 0.64$.

The system of units for the MPCD solvent were the collision cell edge length l, mass m_0 of the solvent particles and the energy scale $\epsilon = k_B T$. The simulation timestep was set to $dt = 0.001\tau$ and the MPCD collision timestep was set to $\Delta t = 0.1\tau$ where $\tau = \sqrt{m_0\, l^2/\epsilon}$. The solvent number density was set to $\rho = 5l^{-3}$. Mass of the rod monomers and sphere vertex particles in the MPCD simulations were set to $m = 5m_0$. The solute (rods/spheres) is coupled with the MPCD solvent through the collision step.

Simulations were performed using HOOMD-blue version 2.9.7[72–75] with azplugins version 0.11.0.[76]

Volume fraction profiles of the colloidal particles were computed by convolving the number density profile, ρ_i, of particle of type i with the Heaviside function, $\theta(r_i - |r - r'|)$, which essentially represents the volume of the sphere of radius r_i, i.e.,[77]

$$\phi_i(\mathrm{r}) = \int d\mathrm{r}'\, \rho_i(|\mathrm{r}'|)\, \theta(r_i - |\mathrm{r} - \mathrm{r}'|) \qquad (10)$$

This integral can be simplified using the radial symmetry of the droplet as,

$$\phi_i(\mathrm{r}) = \frac{1}{\mathrm{r}} \int d\mathrm{r}'\, \rho(\mathrm{r}')\mathrm{r}'\pi[{r_i}^2 - (\mathrm{r} - \mathrm{r}')^2]\theta(r_i - |\mathrm{r} - \mathrm{r}'|) \qquad \mathrm{r} \geq r_i \qquad (11)$$

Since our model for the rods consists of consecutive overlapping monomers, the overlap volume had to be accounted for while computing the volume fractions. For two overlapping spheres of radius R', whose centers are separated by a distance R', the overlap volume is $V' = 5\pi {R'}^3/12$. To approximately account for the overlap, we multiplied the Heaviside function by a constant $b = 1 - \frac{(5/16)\,(N_\mathrm{m}-1)}{N_\mathrm{m}}$ where N_m is the number of monomers making up a rod and the prefactor $(5/16)$ is the ratio of overlap volume to the volume of a monomer.

RESULTS AND DISCUSSION

1. Formation of supraparticles composed of ellipsoids.

The evaporation-induced self-assembly of particles can be described as an advection–diffusion process in confinement. Inside the spherical droplet, the colloidal particles diffuse due to Brownian motion, while the evaporating air–solvent interface creates an effective advection[78] that can accumulate the colloidal particles and create a concentration gradient, provided the drying is fast enough. The relative contributions of advection and diffusion can be characterized by a dimensionless quantity known as the Péclet number Pe, defined in this context as the ratio of the typical diffusion time, $\tau_\mathrm{d} = R_0^2/D_0$, and the evaporation time, $\tau_\mathrm{ev} = R_0/v_\mathrm{ev}$, at the beginning of drying. Here, R_0 is the initial droplet radius, D_0 is the diffusion coefficient of the colloidal particles at infinite dilution, and v_ev is the initial speed of the receding droplet interface. The expression for the Péclet number then reduces to $Pe = \tau_\mathrm{d}/\tau_\mathrm{ev} = v_\mathrm{ev}\, R_0/D_0$. We define $Pe \gg 1$ as the evaporation-limited regime and $Pe \leq 1$ as the diffusion-limited regime. In the following, Pe_e and Pe_s refer to the Péclet numbers for the elongated and spherical particles, respectively.

1 µL droplets containing PS ellipsoids (~1% initial volume fraction) with varying aspect ratios ($\lambda = 4, 6, 11$, corresponding to approximate lengths 0.92 µm, 1.30 µm, and 1.95 µm) were evaporated from superamphiphobic surfaces at different humidity conditions that led to different evaporation rates. The PS particles have -COOH groups on their surface, which leads to an electrostatic double-layer repulsion between them.[41,79] To improve the stability of the dispersions at late stages of drying with elevated salt concentrations, 1 mM of the anionic surfactant sodium dodecyl sulphate (SDS) was added to each dispersion. Due to the repulsive nature of this interaction, the colloidal particles were modeled as nearly hard particles in the simulations (see Methods section for details). At high relative humidity ($\mathrm{RH} = 75\%, 40 \leq Pe_\mathrm{e} \leq 70$), the complete drying of the droplets took about 90 minutes. Each dispersion droplet formed an almost spherical supraparticle at the end of drying [**Figs. 2a, S4**]. At low relative

humidity (RH = 30%, $170 \leq Pe_e \leq 200$), the final supraparticles were not spherical anymore due to buckling near the end of evaporation, which typically occurred from the top [**Figs. 2b, S5**]. Buckling is a common phenomenon caused by mechanical instabilities.[23] The ordering of the ellipsoids on the buckled supraparticle surface resembled that of high humidity, although more ellipsoids were oriented out of plane on the supraparticle surfaces.

Examination of the supraparticle surfaces under SEM showed a short-range lateral ordering of ellipsoids upon drying at high relative humidity [**Fig. 3(a-c)**]. Most of the ellipsoids were oriented in plane on the supraparticle surface. The supraparticle surface with the most out of plane ellipsoids appeared to be the one with the highest aspect ratio ellipsoids ($\lambda = 11$). To quantify ordering of the ellipsoids on the supraparticle surfaces, we computed an orientational order parameter, defined as

$$S^{\dagger}(\boldsymbol{r}_i, \boldsymbol{r}_j) = \langle 2cos^2\theta_{ij} - 1 \rangle \qquad (12)$$

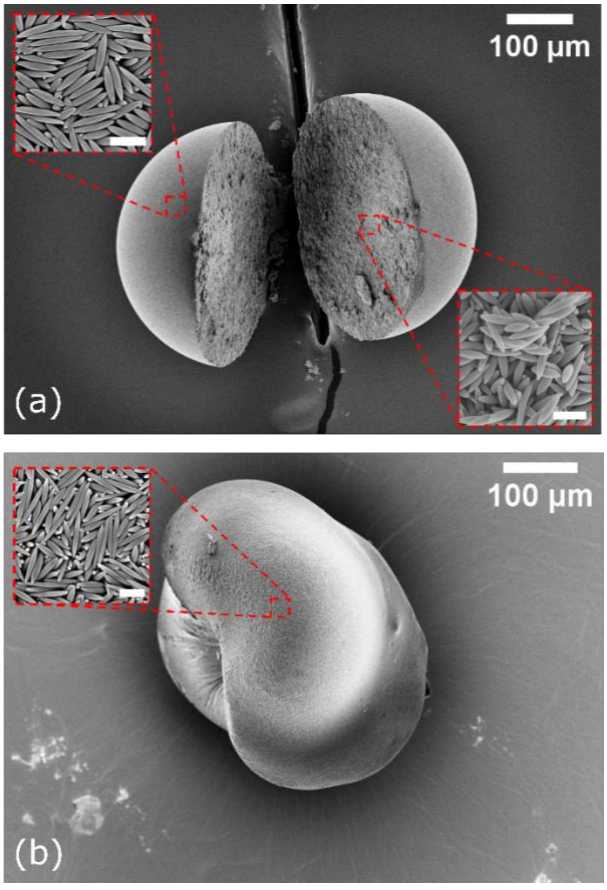

Figure 2. SEM images of supraparticles obtained from evaporation-limited drying with (a) $Pe_e = 50$ and (b) $Pe_e = 170$ for dispersion droplets containing ellipsoids with $\lambda = 6$. Insets show the surface and cross-section of the supraparticles at higher magnification. Scale bar in the insets correspond to 1 µm.

Here, θ_{ij} is the angle between the long axes of two ellipsoids i and j, whose center of masses are separated by distance $r = |\boldsymbol{r}_j - \boldsymbol{r}_i|$ with r_i being the position of ellipsoid i. By construction, a parallel alignment of particles would result in $S^{\dagger} = 1$, while isotropic configurations would yield $S^{\dagger} = 0$. The lateral and longitudinal ordering of the ellipsoids can be best understood when $S^{\dagger}$ is plotted on a spatially resolved two-dimensional heatmap with the width and height

of the cells set approximately equal to the single ellipsoid diameter (d_e) and length (L), respectively [**Fig. 3(d)**], so that adjacent cells represent adjacent ellipsoids. From this plot, we find that, for $\lambda = 11$ ($Pe_e = 70$), the ellipsoids were ordered along the short axis direction up to about four ellipsoid diameters [**Fig. 3(d)**]. For $\lambda = 6$ ($Pe_e = 50$), the ordering along the short axis reduced to three ellipsoid diameters, while no ordering was found for $\lambda = 4$ ($Pe_e = 40$) [**Fig. S6**]. In all cases, the ellipsoids did not exhibit any ordering along their long axis direction. The experiments at low humidity were not used for analyzing the order parameter of the ellipsoids, as many ellipsoids were aligned out of plane on the supraparticle surface.

To understand the extent to which the evaporation rate influenced the surface structure, we performed computer simulations in both the evaporation- and diffusion-limited drying regimes. We first performed simulations with and without hydrodynamic interactions, using droplets with an initial radius of $R_0 = 50d_e$, and found nearly identical structures from both approaches [**Fig. S7**]. This agreement suggests that hydrodynamic interactions play only a negligible role for these systems. Therefore, we primarily performed simulations without hydrodynamic interactions, which allowed us to access larger droplets of radius $R_0 = 100d_e$. Subsequent discussion refers to these simulations.

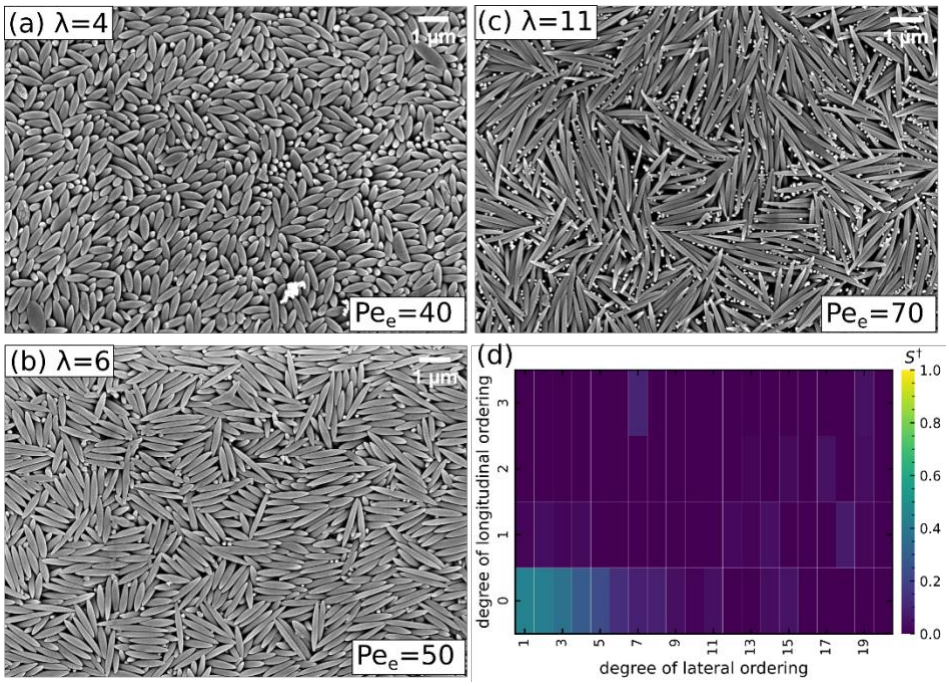

Figure 3. SEM images of supraparticle surface composed of ellipsoids with (a) $\lambda = 4$, (b) $\lambda = 6$ and (c) $\lambda = 11$. Péclet numbers for each case are shown on the bottom right of each panel. (d) 2D heat map for the order parameter $S^\dagger$, computed from the SEM image of the supraparticle surface shown in (c).

The Péclet numbers in simulations and experiments are not exactly identical, but they are on the same order of magnitude, which makes the results comparable. In general, the experimental and simulation results are in good agreement [*cf.* **Figs. 3** and **4**], with some minor differences: The surface SEM images for $\lambda = 11$ [**Fig. 3(c)**] showed some ellipsoids oriented out-of-plane in the experiments, which were absent in the simulation snapshots. This difference might arise from the fact that the simulations treat the ellipsoids as (nearly) hard rods, which might affect their packing. Further, in the simulations, droplet confinement is modeled by a purely repulsive harmonic potential at the droplet-air interface [Eq. (7)], which could suppress an out-of-plane alignment of the colloidal particles.

In the diffusion-limited regime ($Pe_e \leq 1$), the rods showed long-ranged ordering along their short and long axis directions [**Fig. 4(d-f)**], suggesting that the range of surface ordering highly depends on the Péclet numbers. **Figure 4(g)** shows the radially averaged $S^{\dagger}$ for the $\lambda = 11$ rods on the supraparticle surface with varying Péclet numbers. The rods exhibited long-ranged ordering that decayed as the Péclet number increased. The largest Péclet number in our simulations was comparable to that of the experiment at high relative humidity [shown as a dashed line in **Fig. 4(g)**], for which we obtained a similar trend of $S^{\dagger}$. We observed that the range of ordering reduced very quickly with decreasing aspect ratio λ [**Fig. S6**]. For $\lambda = 4$ there was, on average, no lateral ordering of rods.

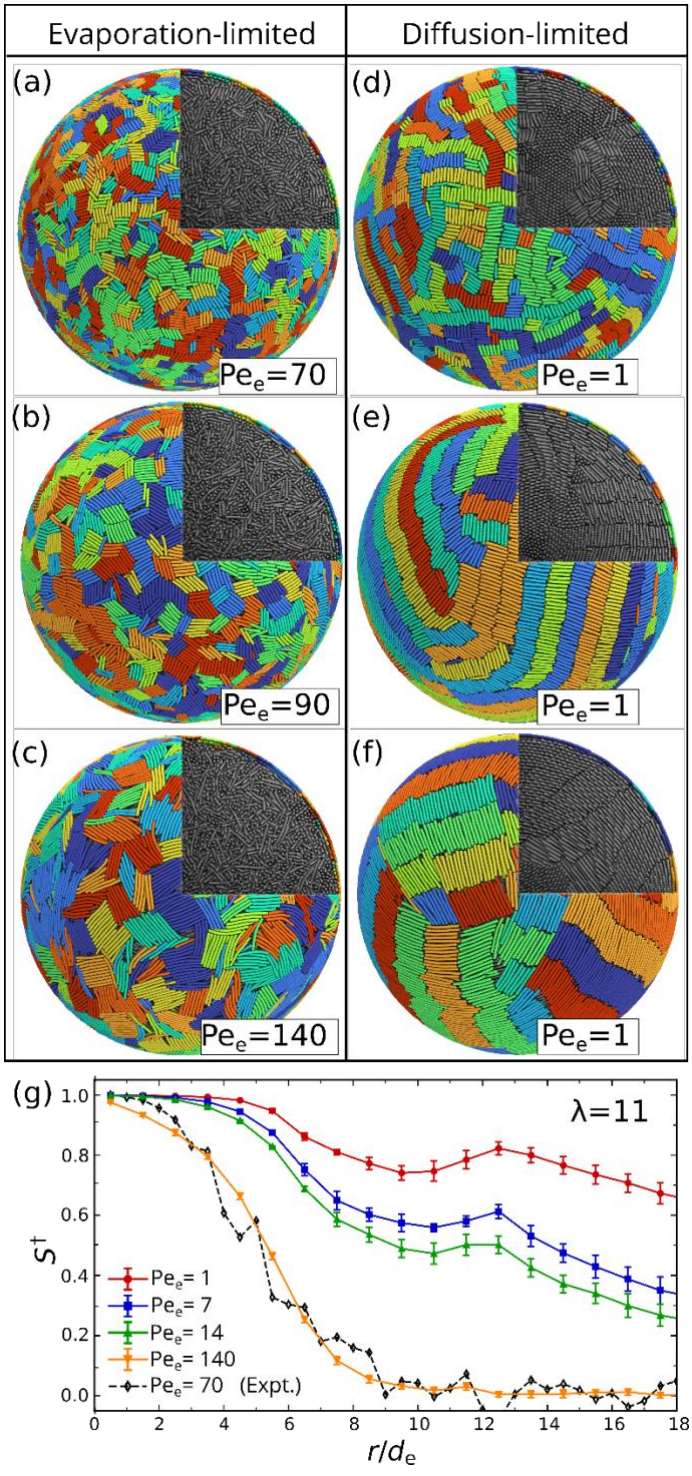

Figure 4. Simulation snapshots showing the supraparticle surface and cross-sections (upper right corner of each snapshot) obtained in the (a-c) evaporation-limited ($Pe_e \gg 1$) and (d-f) diffusion-limited ($Pe_e \leq 1$) drying regimes for $\lambda = 4, 6, 11$. Orientationally ordered clusters of rods on the surface are indicated via different colors for visual aid. (g) $S^{\dagger}$ for $\lambda = 11$ as a function of radial distance on the supraparticle surface for experiments and simulations.

To characterize the ordering of the colloidal particles in the supraparticle interior, the supraparticles were cut in half with a scalpel and imaged using SEM. The images revealed randomly packed ellipsoids regardless of particle aspect ratio [see insets in **Fig.2(a)** and **Fig. S8**]. Since, the packing efficiency of randomly oriented elongated particles is known to decrease with increasing aspect ratio,[48,80–84] we expected an increase in porosity of our supraparticles as we increased λ.

The packing volume fraction ϕ of the colloidal particles was determined as a measure of porosity for the experimental supraparticles by computing the volume of the initial and final droplet *via* image analysis. This was achieved by first determining an arc through the circumference of the 2D image of one half of the droplet, then using the solid of revolution method to compute the volume [**Fig. S3**]. Apart from rotational symmetry, this method does not assume a specific droplet shape and thus avoids systematic errors due to deviation from a perfect sphere. The final particle volume fraction was then calculated as $\phi_f = \phi_0 V_0 / V_f$ where, ϕ_0 is the known initial particle volume fraction and V_0 and V_f are the initial and final droplet volumes, respectively. We computed ϕ_f for all three ellipsoid aspect ratios as well as for spherical particles that served as a reference point (**Table 2**). The final particle volume fraction tended to decrease with increasing ellipsoid aspect ratio λ, which is consistent with simulation studies of randomly packed rods in the bulk.[48,80,84,85] The decrease in random packing efficiency of ellipsoids inside the supraparticles can be attributed to the increase of orientationally averaged excluded volume for particles with higher aspect ratios.[47,48,86] Our results suggest that the supraparticle porosity might then be further increased (ϕ_f decreased) using ellipsoids with higher aspect ratios.

λ	ϕ_0	ϕ_f	Theoretically expected ϕ_f
1	0.011 ± 0.001	0.61 ± 0.06	0.66[48],0.68[84,86],0.69[85]
4	0.011 ± 0.001	0.59 ± 0.03	0.53[48],0.55[84],0.59[80],0.61[85]
6	0.013 ± 0.002	0.57 ± 0.08	0.51[86],0.55[85]
11	0.081 ± 0.001	0.52 ± 0.04	0.40[86],0.43[84],0.44[80],0.48[85]

Table 2. *Final volume fractions of colloidal particles in supraparticles at high relative humidity ($10 \leq Pe_e \leq 70$). The last column shows the theoretically expected values for random packing in bulk dispersions.*

Likewise, the supraparticle cross-sections from simulations in the evaporation-limited regime ($70 \leq Pe_e \leq 140$) showed that the rods were randomly packed in the interior [**Fig. 4(a-c)**]. In contrast, the simulations in the diffusion-limited regime ($Pe_e \leq 1$) exhibited local nematic ordering [**Fig. 4(d-f)**], which can be explained *via* entropic arguments: At sufficiently high concentrations, rods prefer to align nematically to increase the translational entropy at the expense of orientational entropy.[87] The isotropic–nematic transition shifts to lower concentrations with increasing aspect ratios.[88,89] This transition requires the reorientation of individual rods and nematic bundles, which could be suppressed when the droplet is dried quickly ($Pe \gg 1$).

Since the simulation cross-sections indicated the formation of orientationally ordered bundles of rods under certain conditions, we computed the global nematic order parameter in the droplets at various stages of the drying process. To establish a reference for the global nematic ordering of the rods, we performed additional bulk simulations at packing fractions ranging from 0.10 to 0.60 (**Fig. S9**). To ensure proper equilibration, two different approaches were taken when performing the bulk simulations. In the first, we started with a dilute system of randomly oriented rods and compressed the simulation box slowly to reach the desired packing fraction. In the second, we started with an ordered system at high packing fraction and expanded the simulation box slowly. The final ordering in the bulk systems was virtually identical for both approaches, which confirms that the systems were properly equilibrated (**Fig. S10**).

The bulk and confined systems were then analyzed for nematic order using the orientational bond order parameter,[90]

$$Q_{ni}^{\alpha\beta} = \frac{1}{2}\left(3u_{ni}^{\alpha}u_{ni}^{\beta} - \delta_{\alpha\beta}\right) \qquad (14)$$

Here, u_{ni}^{α} is the unit bond vector connecting monomer i and $i+1$ in the n^{th} rod, and $\alpha, \beta \in (x, y, z)$ denote the Cartesian coordinates. The largest eigenvalue S of the tensor $\overline{Q}$, averaged over all bonds gives information of the global nematic order in the system.

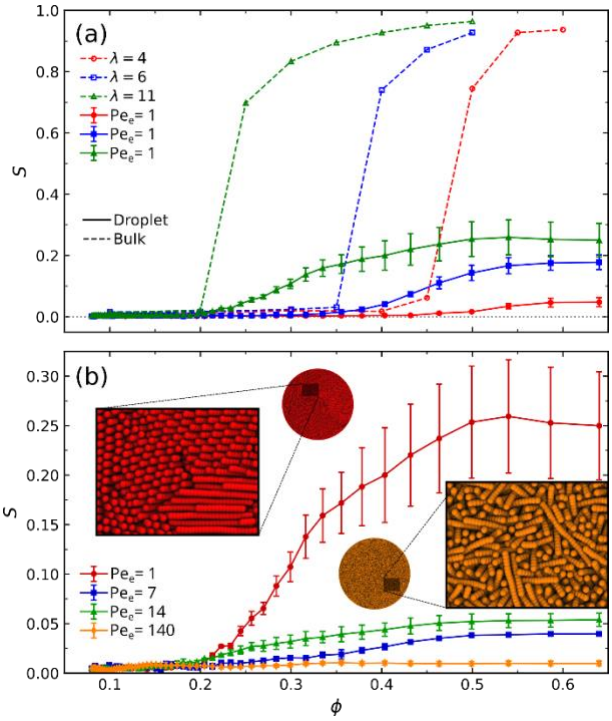

Figure 5. (a) Global nematic order parameter, S, for bulk (open symbols with dashed lines) and diffusion-limited simulations of droplets (filled symbols with solid lines). (b) Péclet number dependence of global nematic order parameter in drying droplet for $\lambda = 11$. Simulation cross-section snapshots of final supraparticles are shown for $Pe_e = 1$ (red) and $Pe_e = 140$ (orange). Lines are guides to the eye only.

We compared the global nematic order in the bulk and drying simulations at low Péclet numbers ($Pe_e \sim 1$) [**Fig. 5(a)**]. In the bulk systems, we observed an isotropic–nematic transition for all aspect ratios λ, where the volume fraction ϕ_{IN} of the transition decreased with increasing λ, as expected. The approximate volume fractions at which the isotropic–nematic transition

occurred were $\phi_{\mathrm{IN}} = 0.475, 0.375, 0.225$ for rods of aspect ratios 4, 6, and 11, respectively. In the case of drying droplets, the long-range nematic ordering of the rods was suppressed due to the confinement, in agreement with previous studies of nematic systems in various confinements.[91–94] However, some smaller nematic bundles formed at volume fractions near ϕ_{IN} of the bulk systems. Since drying of a droplet is essentially a non-equilibrium process, we studied the influence of Péclet number on the long-range nematic ordering of rods in the droplet. **Figure 5(b)** shows for $\lambda = 11$ that the nematic order became even more suppressed with increasing Péclet numbers (data for other λ shown in **Fig. S11**).

2. **Formation of supraparticles composed of sphere–ellipsoid mixtures.**

When evaporating droplets containing PS sphere–ellipsoid mixtures from superamphiphobic surfaces, we obtained almost spherical supraparticles at both low and high relative humidity conditions (**Fig. S4**). The surface SEM images were analyzed by selecting small regions and counting the number of ellipsoids and spheres in those regions. Since particle sizes were known, we could estimate the relative area fractions of the constituent particles, denoted as σ_{e} and σ_{s} for ellipsoids and spheres, respectively (**Fig. 6**).

We characterize the drying conditions of these binary mixtures using two Péclet numbers, namely Pe_{s} for the spherical particles and Pe_{e} for the elongated particles, since the two particle types have different long-time self-diffusion coefficients. Supraparticles made under high humidity conditions ($40 \leq Pe_{\mathrm{e}} \leq 50$ and $Pe_{\mathrm{s}} = 10$) had a surface predominantly occupied by the ellipsoids for all aspect ratios [**Fig. 6(a, c)**]. Under low humidity conditions ($130 \leq Pe_{\mathrm{e}} \leq 200$ and $30 \leq Pe_{\mathrm{s}} \leq 50$), however, the supraparticle surface was occupied by a mixture of ellipsoids and spheres [**Figs. 6(b, d), S12**].

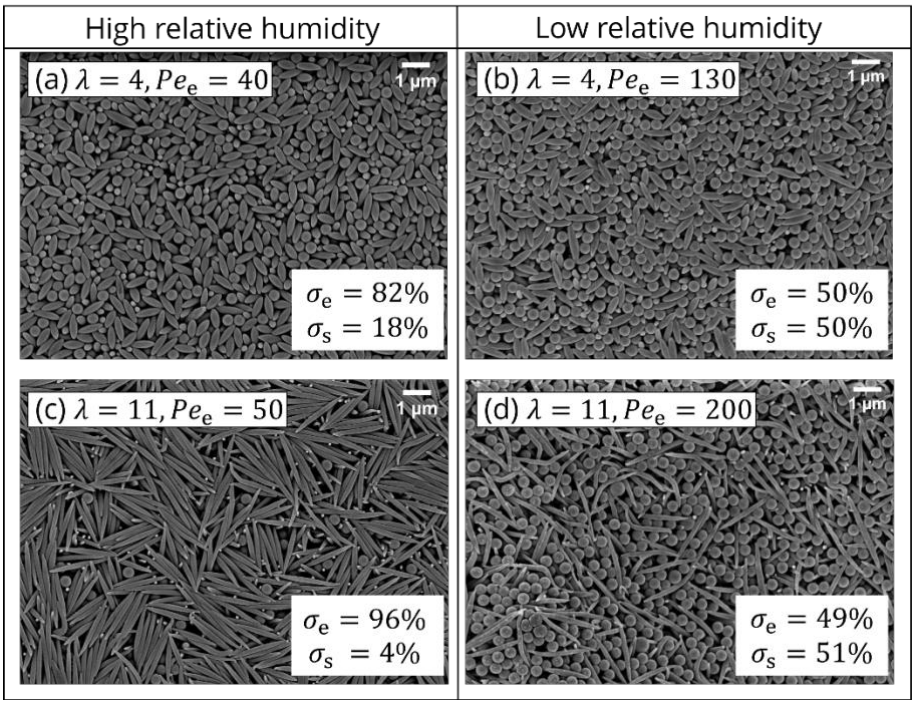

Figure 6. SEM images of the surface of supraparticles composed of sphere–ellipsoid mixtures, with ellipsoids having (a, b) $\lambda = 4$ and (c, d) $\lambda = 11$. (a) & (c) correspond to high relative humidity experiments ($40 \leq Pe_e \leq 50$ and $Pe_s = 10$), while (b) & (d) correspond to low relative humidity ($130 \leq Pe_e \leq 200$ and $30 \leq Pe_s \leq 50$). Fig. S12 shows the supraparticle surfaces for $\lambda = 6$ at low and high relative humidity.

The cross-sectional SEM images indicated a single layer of ellipsoids oriented parallel to the interface under high relative humidity conditions (**Fig. 7**). It was followed by a homogeneous mixture of the ellipsoids and spheres inside the supraparticle, irrespective of the ellipsoid aspect ratio and evaporation rate (**Figs. S13 and S14**). To elucidate the effect of mixing spheres and ellipsoids on the final volume fraction of colloidal particles in the supraparticles, we computed ϕ_f using image analysis of the evaporation videos as described previously. Here, we observed again a decrease in ϕ_f with increasing aspect ratio of the ellipsoids (**Table 3**). This decrease in ϕ_f can be rationalized by the random packing of ellipsoids in our supraparticles, which introduces additional constraints on the packing of spheres. The final particle volume fractions obtained at low relative humidity were slightly smaller than those at high relative humidity. These findings support our hypothesis that fast drying can be leveraged to prevent the systems from relaxing into a close-packed configuration.

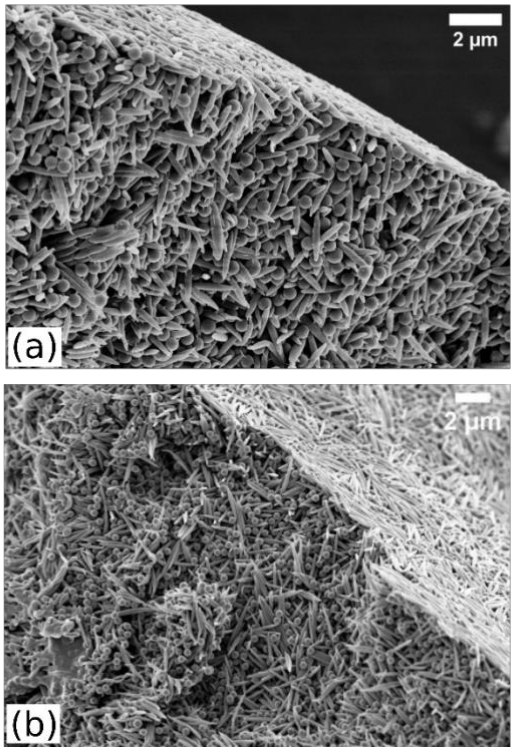

Figure 7. Cross-section SEM images near the surface of the supraparticles which were composed of sphere-ellipsoid mixtures. (a) $\lambda = 6$ at low relative humidity ($Pe_e = 120$ and $Pe_s = 30$) and (b) $\lambda = 11$ at high relative humidity ($Pe_e = 50$ and $Pe_s = 10$).

λ	ϕ_0	ϕ_f high RH	ϕ_f low RH
4	0.0066 ± 0.0002	0.59 ± 0.02	0.54 ± 0.02
6	0.0066 ± 0.0004	0.52 ± 0.03	0.50 ± 0.03
11	0.0066 ± 0.0004	0.48 ± 0.03	0.45 ± 0.03

***Table 3.** Final volume fractions of colloidal particles in supraparticles composed of sphere-ellipsoid mixtures at high relative humidity ($40 \leq Pe_e \leq 50$ and $Pe_s = 10$) and at low relative humidity ($130 \leq Pe_e \leq 200$ and $30 \leq Pe_s \leq 50$).*

Complementary drying simulations of sphere–rod mixtures were performed starting with a total initial volume fraction $\phi_0 = 0.08$, with equal initial volume fractions of rods ($\phi_{0,e}$) and spheres ($\phi_{0,s}$), i.e., $\phi_{0,e} = \phi_{0,s} = 0.04$. As with the pure rod systems, simulations with and

without hydrodynamic interactions did not show any significant differences (**Fig. S15**), suggesting that hydrodynamic interactions between the particles again play a negligible role in these systems. Accordingly, we also performed simulations without hydrodynamics for larger droplets with $R_0 = 100d_e$ to improve statistics.

The sphere and rod volume fractions were computed as a function of radial position in the supraparticle from their respective number density profiles (**Figs. 8 and S16**). **Figure 8** shows the volume-fraction profiles at initial, intermediate, and final stages of drying for rods with $\lambda = 11$, in case of (a) diffusion-limited drying regime ($Pe_e = 1$) and (b) evaporation-limited drying regime ($Pe_e = 140$). For both regimes, a thin shell of rods formed at the supraparticle surface, followed by a region predominantly occupied by spheres. This segregation was observed consistently for all aspect ratios of rods and all drying speeds. This behavior was in contrast with the experiments, where we observed a homogeneous distribution of ellipsoids and spheres on the surface at low relative humidity. Similar differences in the surface structure have been reported previously for supraparticles composed of bidisperse sphere mixtures[5], which have been attributed to the lack of hydrodynamic interactions in most simulation models.[62,63] However, we were able to rule out this effect for our systems, by performing simulations with and without hydrodynamic interactions, which yielded virtually identical results (**Figs. S15 and S16**). Another source for the discrepancy between experiments and simulations could be finite-size effects, given that the ratio between the characteristic size of the supraparticle and the colloidal particles is about 10 for the longest rods in the simulations, whereas the ratio is close to 150 in the experiments. Even with our coarse-grained approach, it is impossible to reach such large size-ratios in the simulations, so we cannot rule out this point entirely. However, our simulations with half initial droplet diameter (and half final supraparticle diameter) showed the same qualitative behavior as the larger droplets [**Fig. S16**]. The difference in surface structure might also stem from the stabilization of the dispersions with SDS, which might lead to interfacial effects that are not captured by the simulation model.

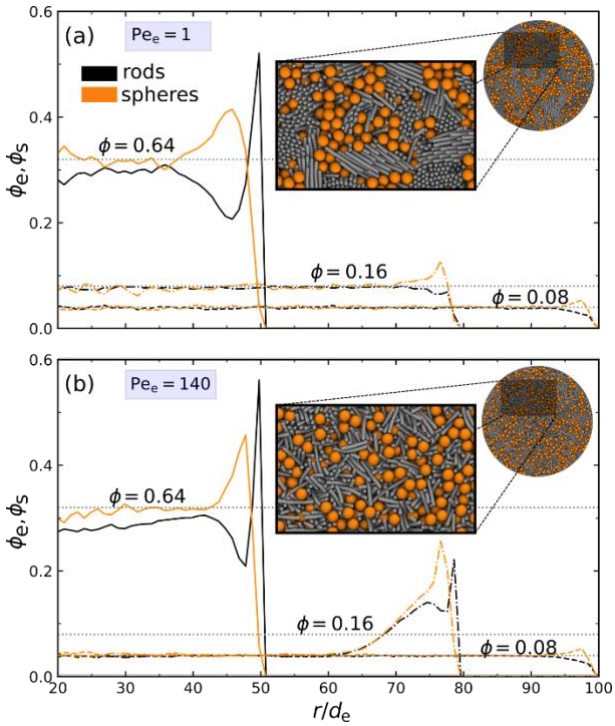

Figure 8. Volume-fraction profiles for mixtures of spheres (ϕ_s, orange) and rods (ϕ_e, black) with $\lambda = 11$, computed from drying simulations with (a) $Pe_e = 1$ (b) $Pe_e = 140$. Dotted gray lines in the plots indicate the total particle

volume fraction in the droplet ϕ when the volume fraction profiles were computed ($\phi = 0.08, 0.16, 0.64$). Insets show cross-sectional snapshots at $\phi = 0.64$.

Visual inspection of the cross-section snapshots in the evaporation-limited drying simulations showed that the interior of the supraparticles consisted of randomly packed rods with spheres filling the interstitial spaces. In contrast, in the diffusion-limited drying regime, the cross-sections showed small nematic bundles of rods along with some randomly packed rods and spheres for aspect ratios 6 and 11. To better understand this behavior, we performed additional bulk simulations of the sphere–rod mixtures with volume fractions ranging from 0.10 to 0.60 using the same equilibration procedure as for the pure rod systems. For the largest aspect ratio, $\lambda = 11$, the mixture started to phase separate at $\phi = 0.4$ and at higher packing fraction, $\phi = 0.5$, the mixture was demixed and the rods were nematically aligned. For the other two cases, $\lambda = 4$ and 6 , the system remained in a mixed phase throughout (**Fig. S17**). We compared the global nematic order in the two bulk simulations – pure rods and sphere–rod mixtures – and observed that the global nematic ordering of the rods was almost completely suppressed in the presence of spheres for $\lambda = 4$ and 6 (**Fig. S18**). In accordance with the observations from the bulk simulations, the drying simulations showed formation of nematic bundles of rods for $\lambda = 11$ in the diffusion-limited drying regime. In comparison with the pure rod systems, global nematic order in the droplets was completely suppressed in the presence of spheres [**Figs. 5(a), S19**].

CONCLUSIONS

We demonstrated that spherical supraparticles could be fabricated using ellipsoidal particles or mixtures of spherical and ellipsoidal particles. We systematically investigated the effect of drying speed on the structure formation and characterized the different drying regimes through the dimensionless Péclet number Pe. In the evaporation-limited drying regime, experiments ($40 \leq Pe_e \leq 70$) and simulations ($70 \leq Pe_e \leq 140$) showed short-range ordering of the ellipsoidal particles on the supraparticle surface and random packing in the interior. In the diffusion-limited regime ($Pe_e \leq 1$), which we could only explore by simulations for practical reasons, we found increased ordering of rods on the supraparticle surface and formation of nematically ordered bundles of rods in the interior. Our findings demonstrate the potential to control the degree of ordering of elongated particles by adjusting their aspect ratio and/or the evaporation rate. The good agreement between experiments and simulations underlines the broad applicability of our strategy. Similar drying experiments can be conducted with, e.g., silica or gold rods for creating supraparticles for various applications, such as sensing or light scattering. Furthermore, the volume fraction of colloidal particles in the final supraparticles decreased with increasing aspect ratio, thus showing a pathway for creating porous supraparticles for catalytic applications.[1]

When forming supraparticles from sphere-ellipsoid mixture at high relative humidity conditions, the supraparticles exhibited an ellipsoid-rich surface monolayer. Simulations indicated an additional sphere-rich region just beneath the surface. This finding hints to the possibility of creating supraparticles with a core-shell morphology by finely tuning the ellipsoid aspect ratio and sphere diameter. Supraparticles made from sphere–ellipsoid mixtures also showed an increase in porosity with increasing ellipsoid aspect ratio. Porosity of these supraparticles could be further increased by subsequently sacrificing the spherical particles, as previously reported for bidisperse sphere mixtures.[1,95] Based on our observations, one could

also fabricate smaller supraparticles that can be used as nanocarriers in specialized applications, such as targeted drug delivery, where the drug itself forms one of the components.

SUPPORTING INFORMATION

Additional SEM images of supraparticles; orientational order parameter plots; schematic explaining solid of revolution method; simulation snapshots of droplets and bulk systems; volume fraction profiles; SEM images of superamphiphobic surfaces and schematic explaining the preparation of PS ellipsoids. Video tracking the morphology of a droplet containing ellipsoids during evaporation at high relative humidity conditions.

ACKNOWLEDGMENTS

This work was funded by the Deutsche Forschungsgemeinschaft (DFG, German Research Foundation) through project numbers 402234552, 405552959, 470113688, 509039598 and the National Science Foundation under Award No. 2223084. Computing time was granted on the supercomputer Mogon at the Johannes Gutenberg University Mainz (www.hpc.uni-mainz.de). We gratefully acknowledge Gabriele Schäfer for synthesizing the colloidal particles, Andreas Hanewald for performing the stretching experiments, and Christine Rosenauer for performing the DLS measurements.

REFERENCES

(1) Liu, W.; Kappl, M.; Butt, H. J. Tuning the Porosity of Supraparticles. *ACS Nano* **2019**, *13* (12), 13949–13956.

(2) Wintzheimer, S.; Granath, T.; Oppmann, M.; Kister, T.; Thai, T.; Kraus, T.; Vogel, N.; Mandel, K. Supraparticles: Functionality from Uniform Structural Motifs. *ACS Nano* **2018**, *12* (6), 5093–5120.

(3) Xia, Y.; Nguyen, T. D.; Yang, M.; Lee, B.; Santos, A.; Podsiadlo, P.; Tang, Z.; Glotzer, S. C.; Kotov, N. A. Self-Assembly of Self-Limiting Monodisperse Supraparticles from Polydisperse Nanoparticles. *Nat Nanotechnol* **2011**, *6* (9), 580–587.

(4) Fujiwara, A.; Wang, J.; Hiraide, S.; Götz, A.; Miyahara, M. T.; Hartmann, M.; Apeleo Zubiri, B.; Spiecker, E.; Vogel, N.; Watanabe, S. Fast Gas Adsorption Kinetics in Supraparticle-Based MOF Packings with Hierarchical Porosity. *Advanced Materials* **2023**, 2305980.

(5) Liu, W.; Midya, J.; Kappl, M.; Butt, H. J.; Nikoubashman, A. Segregation in Drying Binary Colloidal Droplets. *ACS Nano* **2019**, *13* (5), 4972–4979.

(6) Hou, K.; Han, J.; Tang, Z. Formation of Supraparticles and Their Application in Catalysis. *ACS Materials Letters* **2020**, *2* (1), 95–106.

(7) Li, X.; Visaveliya, N.; Hafermann, L.; Gross, G. A.; Knauer, A.; Köhler, J. M. Hierarchically Structured Particles for Micro Flow Catalysis. *Chemical Engineering Journal* **2017**, *326*, 1058–1065.

(8) Oguztürk, H. E.; Bauer, L. J.; Mantouvalou, I.; Kanngieβ er, B.; Velev, O. D.; Gradzielski, M. Preparation of Reinforced Anisometric Patchy Supraparticles for Self-Propulsion. *Particle and Particle Systems Characterization* **2021**, *38* (6), 2000328.

(9) Fang, X. L.; Chen, C.; Jin, M. S.; Kuang, Q.; Xie, Z. X.; Xie, S. Y.; Huang, R. Bin; Zheng, L. S. Single-Crystal-like Hematite Colloidal Nanocrystal Clusters: Synthesis and Applications in Gas Sensors, Photocatalysis and Water Treatment. *J Mater Chem* **2009**, *19* (34), 6154–6160.

(10) Zhao, Y.; Cheng, Y.; Shang, L.; Wang, J.; Xie, Z.; Gu, Z. Microfluidic Synthesis of Barcode Particles for Multiplex Assays. *Small* **2015**, *11* (2), 151–174.

(11) Rial-Hermida, M. I.; Oliveira, N. M.; Concheiro, A.; Alvarez-Lorenzo, C.; Mano, J. F. Bioinspired Superamphiphobic Surfaces as a Tool for Polymer- and Solvent-Independent Preparation of Drug-Loaded Spherical Particles. *Acta Biomater* **2014**, *10* (10), 4314–4322.
(12) Manoharan, V. N.; Imhof, A.; Thorne, J. D.; Pine, D. J. Photonic Crystals from Emulsion Templates. *Advanced Materials* **2001**, *13* (6), 447–450.
(13) Park, J. G.; Kim, S. H.; Magkiriadou, S.; Choi, T. M.; Kim, Y. S.; Manoharan, V. N. Full-Spectrum Photonic Pigments with Non-Iridescent Structural Colors through Colloidal Assembly. *Angewandte Chemie - International Edition* **2014**, *53* (11), 2899–2903.
(14) Vogel, N.; Utech, S.; England, G. T.; Shirman, T.; Phillips, K. R.; Koay, N.; Burgess, I. B.; Kolle, M.; Weitz, D. A.; Aizenberg, J. Color from Hierarchy: Diverse Optical Properties of Micron-Sized Spherical Colloidal Assemblies. *Proc Natl Acad Sci U S A* **2015**, *112* (35), 10845–10850.
(15) Koo, H. J.; Kim, Y. J.; Lee, Y. H.; Lee, W. I.; Kim, K.; Park, N. G. Nano-Embossed Hollow Spherical TiO2 as Bifunctional Material for High-Efficiency Dye-Sensitized Solar Cells. *Advanced Materials* **2008**, *20* (1), 195–199.
(16) Li, X.; Gu, M.; Hu, S.; Kennard, R.; Yan, P.; Chen, X.; Wang, C.; Sailor, M. J.; Zhang, J. G.; Liu, J. Mesoporous Silicon Sponge as an Anti-Pulverization Structure for High-Performance Lithium-Ion Battery Anodes. *Nat Commun* **2014**, *5*, 1–7.
(17) Han, J.; Zhang, X.; Zhou, Y.; Ning, Y.; Wu, J.; Liang, S.; Sun, H.; Zhang, H.; Yang, B. Fabrication of CdTe Nanoparticles-Based Superparticles for an Improved Detection of Cu 2+ and Ag +. *J Mater Chem* **2012**, *22* (6), 2679–2686.
(18) Dinsmore, A. D.; Hsu, M. F.; Nikolaides, M. G.; Marquez, Manuel; Bausch, A. R.; Weitz, D A. Colloidosomes: Selectively Permeable Capsules Composed of Colloidal Particles. *Science* **2002**, *298* (5595), 1006–1009.
(19) Velev, O. D.; Furusawa, K; Nagayama, K. Assembly of Latex Particles by Using Emulsion Droplets as Templates. 1. Microstructured Hollow Spheres. *Langmuir* **1996**, *12* (10), 2374–2384.
(20) Hsu, M. F.; Nikolaides, M. G.; Dinsmore, A. D.; Bausch, A. R.; Gordon, V. D.; Chen, X.; Hutchinson, J. W.; Weitz, D. A.; Marquez, M. Self-Assembled Shells Composed of Colloidal Particles: Fabrication and Characterization. *Langmuir* **2005**, *21* (7), 2963–2970.
(21) Rastogi, V.; Melle, S.; Calderón, O. G.; García, A. A.; Marquez, M.; Velev, O. D. Synthesis of Light-Diffracting Assemblies from Microspheres and Nanoparticles in Droplets on a Superhydrophobic Surface. *Advanced Materials* **2008**, *20* (22), 4263–4268.
(22) Lintingre, E.; Ducouret, G.; Lequeux, F.; Olanier, L.; Périé, T.; Talini, L. Controlling the Buckling Instability of Drying Droplets of Suspensions through Colloidal Interactions. *Soft Matter* **2015**, *11* (18), 3660–3665.
(23) Tsapis, N.; Dufresne, E. R.; Sinha, S. S.; Riera, C. S.; Hutchinson, J. W.; Mahadevan, L.; Weitz, D. A. Onset of Buckling in Drying Droplets of Colloidal Suspensions. *Phys Rev Lett* **2005**, *94* (1), 018302.
(24) Bahadur, J.; Sen, D.; Mazumder, S.; Paul, B.; Bhatt, H.; Singh, S. G. Control of Buckling in Colloidal Droplets during Evaporation-Induced Assembly of Nanoparticles. *Langmuir* **2012**, *28* (3), 1914–1923.
(25) Sen, D.; Mazumder, S.; Melo, J. S.; Khan, A.; Bhattyacharya, S.; D'Souza, S. F. Evaporation Driven Self-Assembly of a Colloidal Dispersion during Spray Drying: Volume Fraction Dependent Morphological Transition. *Langmuir* **2009**, *25* (12), 6690–6695.
(26) Bahadur, J.; Sen, D.; Mazumder, S.; Bhattacharya, S.; Frielinghaus, H.; Goerigk, G. Origin of Buckling Phenomenon during Drying of Micrometer-Sized Colloidal Droplets. *Langmuir* **2011**, *27* (13), 8404–8414.
(27) Mondal, R.; Das, A.; Sen, D.; Satapathy, D. K.; Basavaraj, M. G. Spray Drying of Colloidal Dispersions Containing Ellipsoids. *J Colloid Interface Sci* **2019**, *551*, 242–250.
(28) Biswas, P.; Sen, D.; Mazumder, S.; Basak, C. B.; Doshi, P. Temperature Mediated Morphological Transition during Drying of Spray Colloidal Droplets. *Langmuir* **2016**, *32* (10), 2464–2473.

(29) Gharsallaoui, A.; Roudaut, G.; Chambin, O.; Voilley, A.; Saurel, R. Applications of Spray-Drying in Microencapsulation of Food Ingredients: An Overview. *Food Research International* **2007**, *40* (9), 1107–1121.
(30) Sen, D.; Spalla, O.; Taché, O.; Haltebourg, P.; Thill, A. Slow Drying of a Spray of Nanoparticles Dispersion. in Situ SAXS Investigation. *Langmuir* **2007**, *23* (8), 4296–4302.
(31) Agthe, M.; Plivelic, T. S.; Labrador, A.; Bergström, L.; Salazar-Alvarez, G. Following in Real Time the Two-Step Assembly of Nanoparticles into Mesocrystals in Levitating Drops. *Nano Lett* **2016**, *16* (11), 6838–6843.
(32) Liu, Z.; Liu, Y.; Yang, J.; Li, S.; Peng, C.; Cui, X.; Sheng, L.; Wu, B. Highly Efficient and Controlled Fabrication of Supraparticles by Leidenfrost Phenomenon. *Langmuir* **2022**, *38* (30), 9157–9165.
(33) Chu, Z.; Seeger, S. Superamphiphobic Surfaces. *Chemical Society Reviews* **2014**, *43* (8), 2784–2798.
(34) Kota, A. K.; Choi, W.; Tuteja, A. Superomniphobic Surfaces: Design and Durability. *MRS Bull* **2013**, *38* (5), 383–390.
(35) Zhang, J.; Seeger, S. Superoleophobic Coatings with Ultralow Sliding Angles Based on Silicone Nanofilaments. *Angewandte Chemie - International Edition* **2011**, *50* (29), 6652–6656.
(36) Butt, H. J.; Semprebon, C.; Papadopoulos, P.; Vollmer, D.; Brinkmann, M.; Ciccotti, M. Design Principles for Superamphiphobic Surfaces. *Soft Matter* **2013**, *9* (2), 418–428.
(37) Deegan, R. D.; Bakajin, O.; Huber, G.; Nagel, S. R.; Witten, T. A. Capillary Flow as the Cause of Ring. *Nature* **1997**, *389*, 827–829.
(38) Pan, Z.; Dash, S.; Weibel, J. A.; Garimella, S. V. Assessment of Water Droplet Evaporation Mechanisms on Hydrophobic and Superhydrophobic Substrates. *Langmuir* **2013**, *29* (51), 15831–15841.
(39) Pham, T.; Kumar, S. Drying of Droplets of Colloidal Suspensions on Rough Substrates. *Langmuir* **2017**, *33* (38), 10061–10076.
(40) Tan, H.; Diddens, C.; Versluis, M.; Butt, H. J.; Lohse, D.; Zhang, X. Self-Wrapping of an Ouzo Drop Induced by Evaporation on a Superamphiphobic Surface. *Soft Matter* **2017**, *13* (15), 2749–2759.
(41) Liu, W.; Kappl, M.; Steffen, W.; Butt, H. J. Controlling Supraparticle Shape and Structure by Tuning Colloidal Interactions. *J Colloid Interface Sci* **2022**, *607*, 1661–1670.
(42) Wooh, S.; Huesmann, H.; Tahir, M. N.; Paven, M.; Wichmann, K.; Vollmer, D.; Tremel, W.; Papadopoulos, P.; Butt, H. J. Synthesis of Mesoporous Supraparticles on Superamphiphobic Surfaces. *Advanced Materials* **2015**, *27* (45), 7338–7343.
(43) Deng, X.; Paven, M.; Papadopoulos, P.; Ye, M.; Wu, S.; Schuster, T.; Klapper, M.; Vollmer, D.; Butt, H. J. Solvent-Free Synthesis of Microparticles on Superamphiphobic Surfaces. *Angewandte Chemie - International Edition* **2013**, *52* (43), 11286–11289.
(44) Glotzer, S. C.; Solomon, M. J. Anisotropy of Building Blocks and Their Assembly into Complex Structures. *Nature Mater* **2007**, *6*, 557–562.
(45) Schyck, S.; Meijer, J. M.; Baldauf, L.; Schall, P.; Petukhov, A. V.; Rossi, L. Self-Assembly of Colloidal Superballs under Spherical Confinement of a Drying Droplet. *JCIS Open* **2022**, *5*, 100037.
(46) Marino, E.; Van Dongen, S. W.; Neuhaus, S. J.; Li, W.; Keller, A. W.; Kagan, C. R.; Kodger, T. E.; Murray, C. B. Monodisperse Nanocrystal Superparticles Through a Source-Sink Emulsion System. *Chemistry of Materials* **2022**, *34* (6), 2779–2789.
(47) Philipse, A. P. The Random Contact Equation and Its Implications for (Colloidal) Rods in Packings, Suspensions, and Anisotropic Powders. *Langmuir* **1996**, *12* (5), 1127–1133.
(48) Williams, S. R.; Philipse, A. P. Random Packings of Spheres and Spherocylinders Simulated by Mechanical Contraction. *Phys Rev E Stat Phys Plasmas Fluids Relat Interdiscip Topics* **2003**, *67* (5), 9.

(49) Jungblut, S.; Binder, K.; Schilling, T. Isotropic-Isotropic Phase Separation in Mixtures of Rods and Spheres: Some Aspects of Monte Carlo Simulation in the Grand Canonical Ensemble. *Comput Phys Commun* **2008**, *179* (1–3), 13–16.
(50) Kyrylyuk, A. V.; Anne Van De Haar, M.; Rossi, L.; Wouterse, A.; Philipse, A. P. Isochoric Ideality in Jammed Random Packings of Non-Spherical Granular Matter. *Soft Matter* **2011**, *7* (5), 1671–1674.
(51) Jacucci, G.; Longbottom, B. W.; Parkins, C. C.; Bon, S. A. F.; Vignolini, S. Anisotropic Silica Colloids for Light Scattering. *J Mater Chem C Mater* **2021**, *9* (8), 2695–2700.
(52) van der Hoeven, J. E. S.; Gurunarayanan, H.; Bransen, M.; de Winter, D. A. M.; de Jongh, P. E.; van Blaaderen, A. Silica-Coated Gold Nanorod Supraparticles: A Tunable Platform for Surface Enhanced Raman Spectroscopy. *Adv Funct Mater* **2022**, *32* (27), 2200148.
(53) Wang, D.; Hermes, M.; Najmr, S.; Tasios, N.; Grau-Carbonell, A.; Liu, Y.; Bals, S.; Dijkstra, M.; Murray, C. B.; van Blaaderen, A. Structural Diversity in Three-Dimensional Self-Assembly of Nanoplatelets by Spherical Confinement. *Nat Commun* **2022**, *13* (1), 6001.
(54) Shouldice, G. T. D.; Vandezande, G. A.; Rudin, A. Practical Aspects of the Emulsifier-Free Emulsion Polymerization of Styrene. *Eur Polym J* **1994**, *30* (2), 179–183.
(55) Geyer, F.; Schönecker, C.; Butt, H. J.; Vollmer, D. Enhancing CO2 Capture Using Robust Superomniphobic Membranes. *Advanced Materials* **2017**, *29* (5), 1603524.
(56) Ho, C. C.; Keller, A.; Odell, J. A.; Ottewill, R. H. Preparation of Monodisperse Ellipsoidal Polystyrene Particles. *Colloid Polym Sci* **1993**, *271* (5), 469–479.
(57) Howard, M. P.; Reinhart, W. F.; Sanyal, T.; Shell, M. S.; Nikoubashman, A.; Panagiotopoulos, A. Z. Evaporation-Induced Assembly of Colloidal Crystals. *Journal of Chemical Physics* **2018**, *149* (9), 094901.
(58) Tang, Y.; Grest, G. S.; Cheng, S. Stratification of Drying Particle Suspensions: Comparison of Implicit and Explicit Solvent Simulations. *Journal of Chemical Physics* **2019**, *150* (22), 224901.
(59) Tang, Y.; Grest, G. S.; Cheng, S. Stratification in Drying Films Containing Bidisperse Mixtures of Nanoparticles. *Langmuir* **2018**, *34* (24), 7161–7170.
(60) Fortini, A.; Martín-Fabiani, I.; De La Haye, J. L.; Dugas, P.-Y.; Lansalot, M.; D'Agosto, F.; Bourgeat-Lami, E.; Keddie, J. L.; Sear, R. P. Dynamic Stratification in Drying Films of Colloidal Mixtures. *Phys. Rev. Lett.* **2016**, *116* (11), 118301.
(61) Makepeace, D. K.; Fortini, A.; Markov, A.; Locatelli, P.; Lindsay, C.; Moorhouse, S.; Lind, R.; Sear, R. P.; Keddie, J. L. Stratification in Binary Colloidal Polymer Films: Experiment and Simulations. *Soft Matter* **2017**, *13* (39), 6969–6980.
(62) Statt, A.; Howard, M. P.; Panagiotopoulos, A. Z. Influence of Hydrodynamic Interactions on Stratification in Drying Mixtures. *Journal of Chemical Physics* **2018**, *149* (2), 024902.
(63) Sear, R. P.; Warren, P. B. Diffusiophoresis in Nonadsorbing Polymer Solutions: The Asakura-Oosawa Model and Stratification in Drying Films. *Phys Rev E* **2017**, *96* (6), 062602.
(64) Howard, M. P.; Nikoubashman, A. Stratification of Polymer Mixtures in Drying Droplets: Hydrodynamics and Diffusion. *Journal of Chemical Physics* **2020**, *153* (5), 054901.
(65) Malevanets, A.; Kapral, R. Mesoscopic Model for Solvent Dynamics. *J Chem Phys* **1999**, *110* (17), 8605–8613.
(66) Ihle, T.; Kroll, D. M. Stochastic Rotation Dynamics: A Galilean-Invariant Mesoscopic Model for Fluid Flow. *Phys Rev E* **2001**, *63* (2), 020201.
(67) Gompper, G.; Ihle, T.; Kroll, D. M.; Winkler, R. G. Multi-Particle Collision Dynamics: A Particle-Based Mesoscale Simulation Approach to the Hydrodynamics of Complex Fluids. In *Advanced Computer Simulation Approaches for Soft Matter Sciences III*; Springer Berlin Heidelberg: Berlin, Heidelberg 2009; pp 1–87.
(68) Aponte-Rivera, C.; Zia, R. N. Simulation of Hydrodynamically Interacting Particles Confined by a Spherical Cavity. *Phys Rev Fluids* **2016**, *1* (2), 023301.

(69) Wani, Y. M.; Kovakas, P. G.; Nikoubashman, A.; Howard, M. P. Diffusion and Sedimentation in Colloidal Suspensions Using Multiparticle Collision Dynamics with a Discrete Particle Model. *J. Chem. Phys.* **2022**, *156* (2), 024901.
(70) Poblete, S.; Wysocki, A.; Gompper, G.; Winkler, R. G. Hydrodynamics of Discrete-Particle Models of Spherical Colloids: A Multiparticle Collision Dynamics Simulation Study. *Phys Rev E* **2014**, *90* (3), 033314.
(71) Winkler, R. G.; Mussawisade, K.; Ripoll, M.; Gompper, G. Rod-like Colloids and Polymers in Shear Flow: A Multi-Particle-Collision Dynamics Study. *Journal of Physics: Condensed Matter* **2004**, *16* (38), 3941–3954.
(72) Howard, M. P.; Panagiotopoulos, A. Z.; Nikoubashman, A. Efficient Mesoscale Hydrodynamics: Multiparticle Collision Dynamics with Massively Parallel GPU Acceleration. *Comput Phys Commun* **2018**, *230*, 10–20.
(73) Anderson, J. A.; Glaser, J.; Glotzer, S. C. HOOMD-Blue: A Python Package for High-Performance Molecular Dynamics and Hard Particle Monte Carlo Simulations. *Comput Mater Sci* **2020**, *173*, 109363.
(74) Howard, M. P.; Anderson, J. A.; Nikoubashman, A.; Glotzer, S. C.; Panagiotopoulos, A. Z. Efficient Neighbor List Calculation for Molecular Simulation of Colloidal Systems Using Graphics Processing Units. *Comput Phys Commun* **2016**, *203*, 45–52.
(75) Howard, M. P.; Statt, A.; Madutsa, F.; Truskett, T. M.; Panagiotopoulos, A. Z. Quantized Bounding Volume Hierarchies for Neighbor Search in Molecular Simulations on Graphics Processing Units. *Comput Mater Sci* **2019**, *164*, 139–146.
(76) Howard,M. https://github.com/mphowardlab/azplugins (February 2, 2022).
(77) Roth, R. Fundamental Measure Theory for Hard-Sphere Mixtures: A Review. *Journal of Physics Condensed Matter*. **2010**, *22* (6), 063102.
(78) Routh, A. F.; Zimmerman, W. B. Distribution of Particles during Solvent Evaporation from Films. *Chem Eng Sci* **2004**, *59* (14), 2961–2968.
(79) Israelachvili J.N. Intermolecular and Surface Forces, 3rd ed.; Elsevier: Amsterdam, 2011.
(80) Ferreiro-Córdova, C.; Van Duijneveldt, J. S. Random Packing of Hard Spherocylinders. *J Chem Eng Data* **2014**, *59* (10), 3055–3060.
(81) Man, W.; Donev, A.; Stillinger, F. H.; Sullivan, M. T.; Russel, W. B.; Heeger, D.; Inati, S.; Torquato, S.; Chaikin, P. M. Experiments on Random Packings of Ellipsoids. *Phys Rev Lett* **2005**, *94* (19), 198001.
(82) Young, D. A.; Thomsen, C.; Grahn, H. T.; Maris, H. J.; Donev, A.; Cisse, I.; Sachs, D.; Variano, E. A.; Stillinger, F. H.; Connelly, R.; Torquato, S.; Chaikin, P. M. Improving the Density of Jammed Disordered Packings Using Ellipsoids. *Science* **2004**, *303* (5660), 990–993.
(83) Mukhija, D.; Solomon, M. J. Nematic Order in Suspensions of Colloidal Rods by Application of a Centrifugal Field. *Soft Matter* **2011**, *7* (2), 540–545.
(84) Wouterse, A.; Williams, S. R.; Philipse, A. P. Effect of Particle Shape on the Density and Microstructure of Random Packings. *Journal of Physics Condensed Matter* **2007**, *19* (40), 406215.
(85) Zhao, J.; Li, S.; Zou, R.; Yu, A. Dense Random Packings of Spherocylinders. *Soft Matter* **2012**, *8* (4), 1003–1009.
(86) Kyrylyuk, A. V.; Philipse, A. P. Effect of Particle Shape on the Random Packing Density of Amorphous Solids. *Physica Status Solidi (A) Applications and Materials Science* **2011**, *208* (10), 2299–2302.
(87) Priestley, E. B.; Wojtowicz, P. J.; Sheng, P. *Introduction to Liquid Crystals*; Springer US: Boston, MA, 1975.
(88) Bolhuis, P.; Frenkel, D. Tracing the Phase Boundaries of Hard Spherocylinders. *Journal of Chemical Physics* **1997**, *106* (2), 666–687.
(89) Gschwind, A.; Klopotek, M.; Ai, Y.; Oettel, M. Isotropic-Nematic Transition for Hard Rods on a Three-Dimensional Cubic Lattice. *Phys Rev E* **2017**, *96* (1), 012104.

(90) Khadilkar, M. R.; Nikoubashman, A. Self-Assembly of Semiflexible Polymers Confined to Thin Spherical Shells. *Soft Matter* **2018**, *14* (33), 6903–6911.
(91) Trukhina, Y.; Schilling, T. Computer Simulation Study of a Liquid Crystal Confined to a Spherical Cavity. *Phys Rev E Stat Nonlin Soft Matter Phys* **2008**, *77* (1), 011701.
(92) Monderkamp, P. A.; Wittmann, R.; te Vrugt, M.; Voigt, A.; Wittkowski, R.; Löwen, H. Topological Fine Structure of Smectic Grain Boundaries and Tetratic Disclination Lines within Three-Dimensional Smectic Liquid Crystals. *Physical Chemistry Chemical Physics* **2022**, *24* (26), 15691–15704.
(93) Gârlea, I. C.; Mulder, P.; Alvarado, J.; Dammone, O.; Aarts, D. G. A. L.; Lettinga, M. P.; Koenderink, G. H.; Mulder, B. M. Finite Particle Size Drives Defect-Mediated Domain Structures in Strongly Confined Colloidal Liquid Crystals. *Nat Commun* **2016**, *7,* 12112.
(94) Yao, X.; Chen, J. Z. Y. Rodlike Molecules in Extreme Confinement. *Phys Rev E* **2020**, *101* (6), 062706.
(95) Egly, S.; Fröhlich, C.; Vogel, S.; Gruenewald, A.; Wang, J.; Detsch, R.; Boccaccini, A. R.; Vogel, N. Bottom-Up Assembly of Silica and Bioactive Glass Supraparticles with Tunable Hierarchical Porosity. *Langmuir* **2018**, *34* (5), 2063–2072.

“TOC graphic”

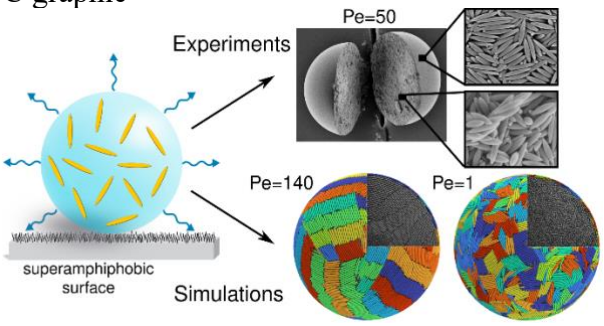
Pe=50
Experiments
Pe=140
Pe=1
superamphiphobic
surface
Simulations

Supporting Information

Structure Formation in Supraparticles Composed of Spherical and Elongated Particles

Melis Yetkin[1+], Yashraj M. Wani[2*], Kritika Kritika[2,3,4], Michael P. Howard[5], Michael Kappl[1], Hans-Jürgen Butt[1], Arash Nikoubashman[2,3,4]

[1]Max-Planck Institute for Polymer Research, Mainz, Germany
[2]Institute of Physics, Johannes Gutenberg University of Mainz, Staudingerweg 7, 55128 Mainz, Germany
[3]Leibniz-Institut für Polymerforschung Dresden e.V., Hohe Straße 6, 01069 Dresden, Germany
[4]Institut für Theoretische Physik, Technische Universität Dresden, 01069 Dresden, Germany
[5]Department of Chemical Engineering, Auburn University, Auburn, Alabama 36849, USA

*These authors contributed equally to this work.

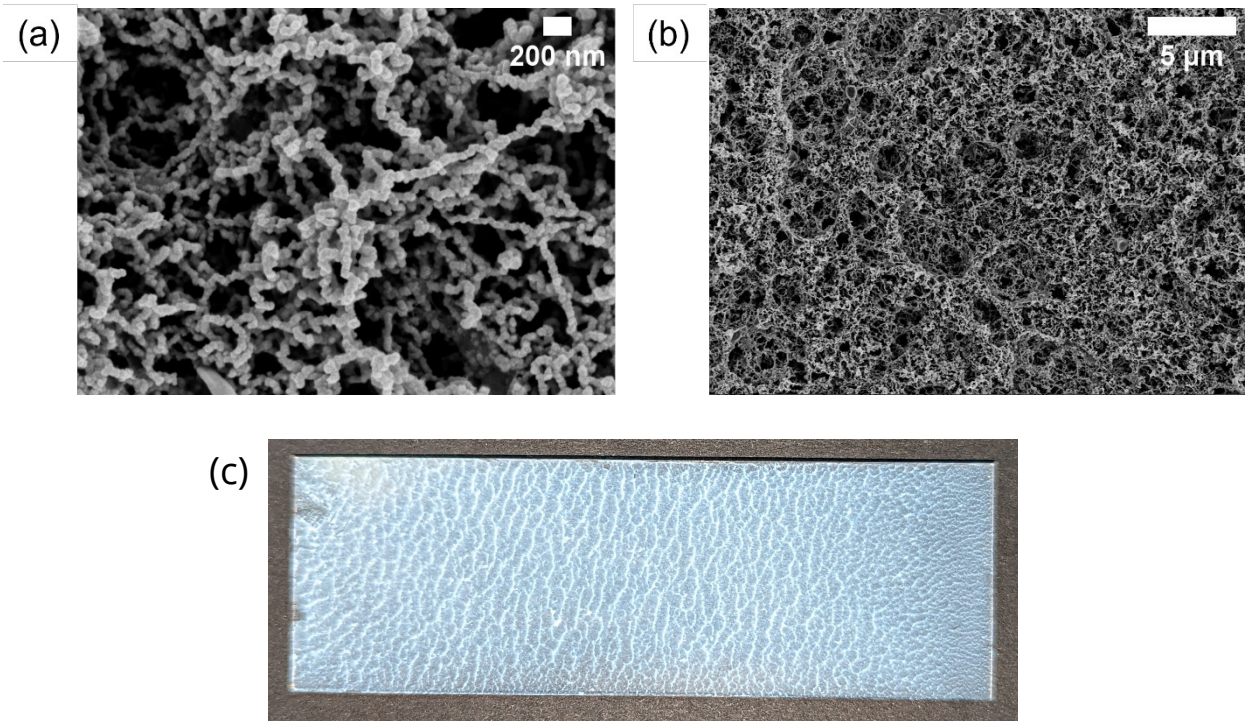

Fig. S1: (a) zoom-in and (b) zoom-out SEM images showing the surface morphology of silicone nanofilament-coated glass substrates (c) photo of the substrate.

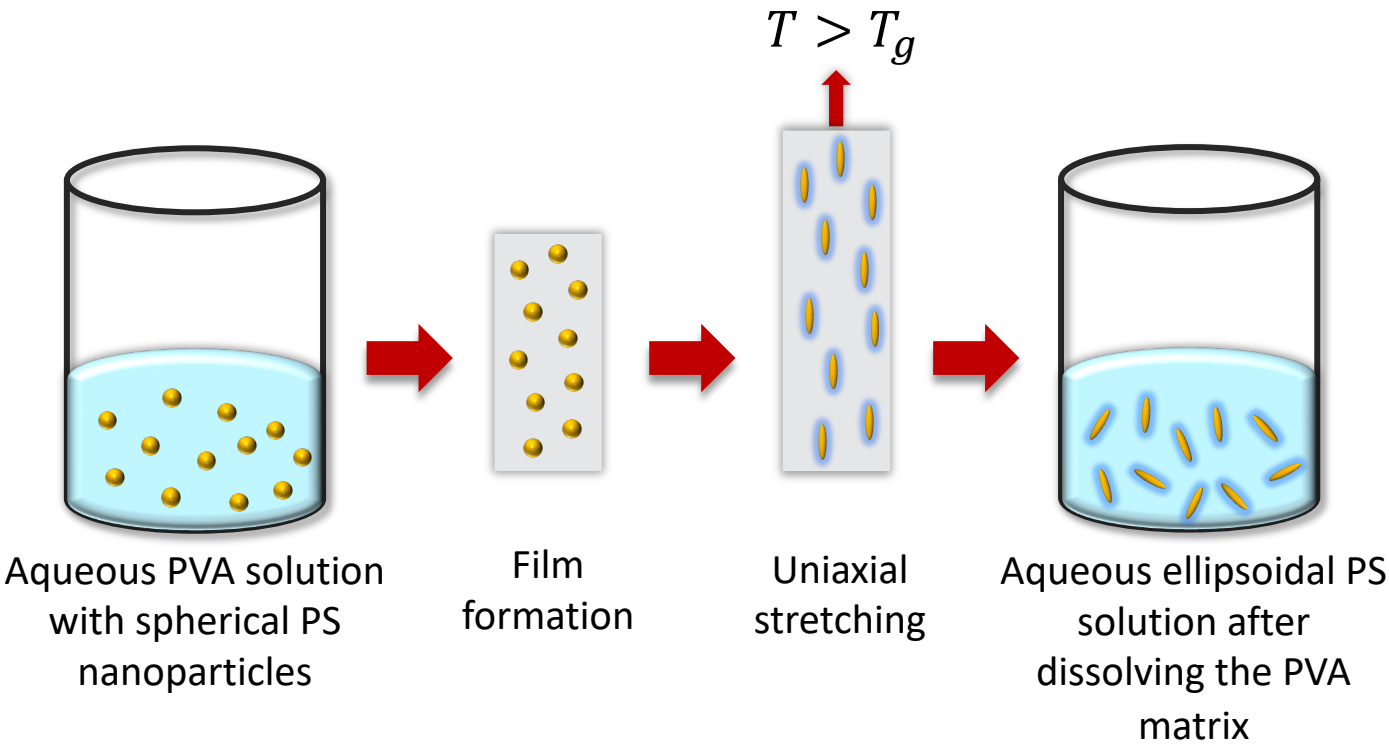

Fig. S2: Schematic depicting the preparation of polystyrene (PS) ellipsoids.

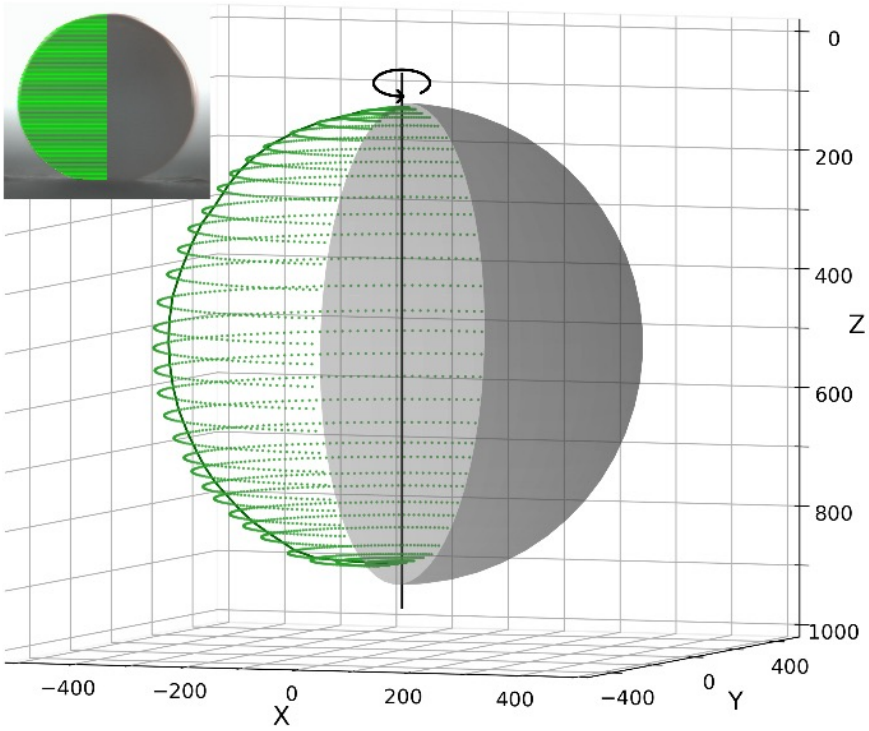

Fig. S3: 3D reconstruction of droplet using solid of revolution (green) compared with a sphere (gray). The inset shows an image of a droplet, in which disc-shape slices are determined for performing solid of revolution.

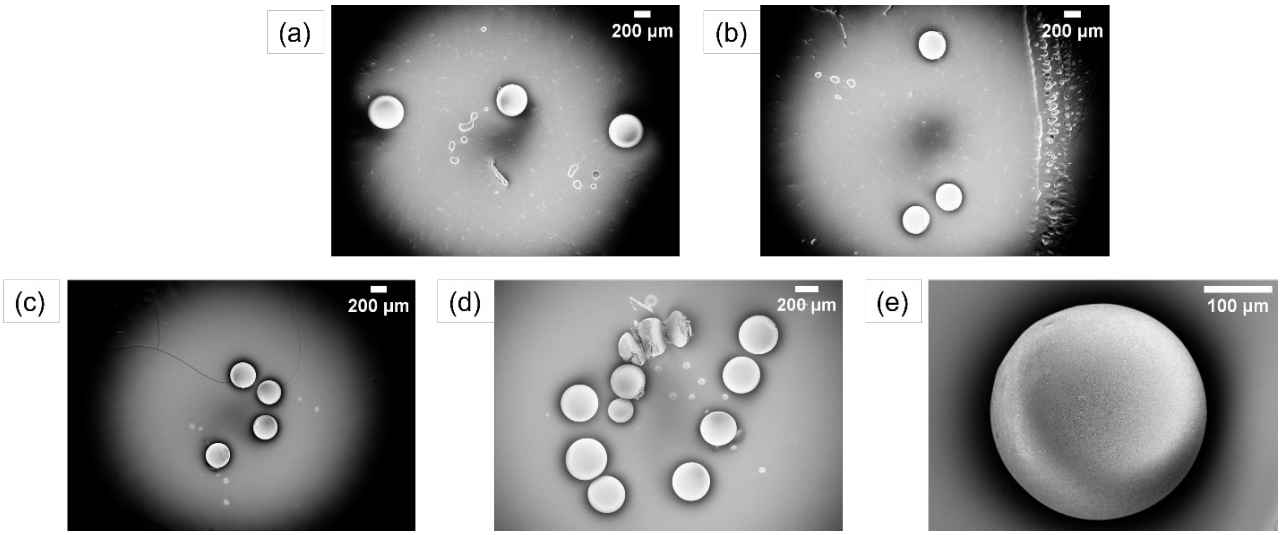

Fig. S4: SEM images showing the spherical final morphology of supraparticles composed of ellipsoids of (a) $\lambda = 6$ at $Pe_{\mathrm{e}} = 50$ (b) $\lambda = 11$ at $Pe_{\mathrm{e}} = 70$ and sphere-ellipsoid mixtures with ellipsoids of (c) $\lambda = 4$ at $Pe_{\mathrm{s}} = 10$ and $Pe_{\mathrm{e}} = 40$ (d) $\lambda = 4$ at $Pe_{\mathrm{s}} = 30$ and $Pe_{\mathrm{e}} = 130$ (e) $\lambda = 11$ at $Pe_{\mathrm{s}} = 10$ and $Pe_{\mathrm{e}} = 50$.

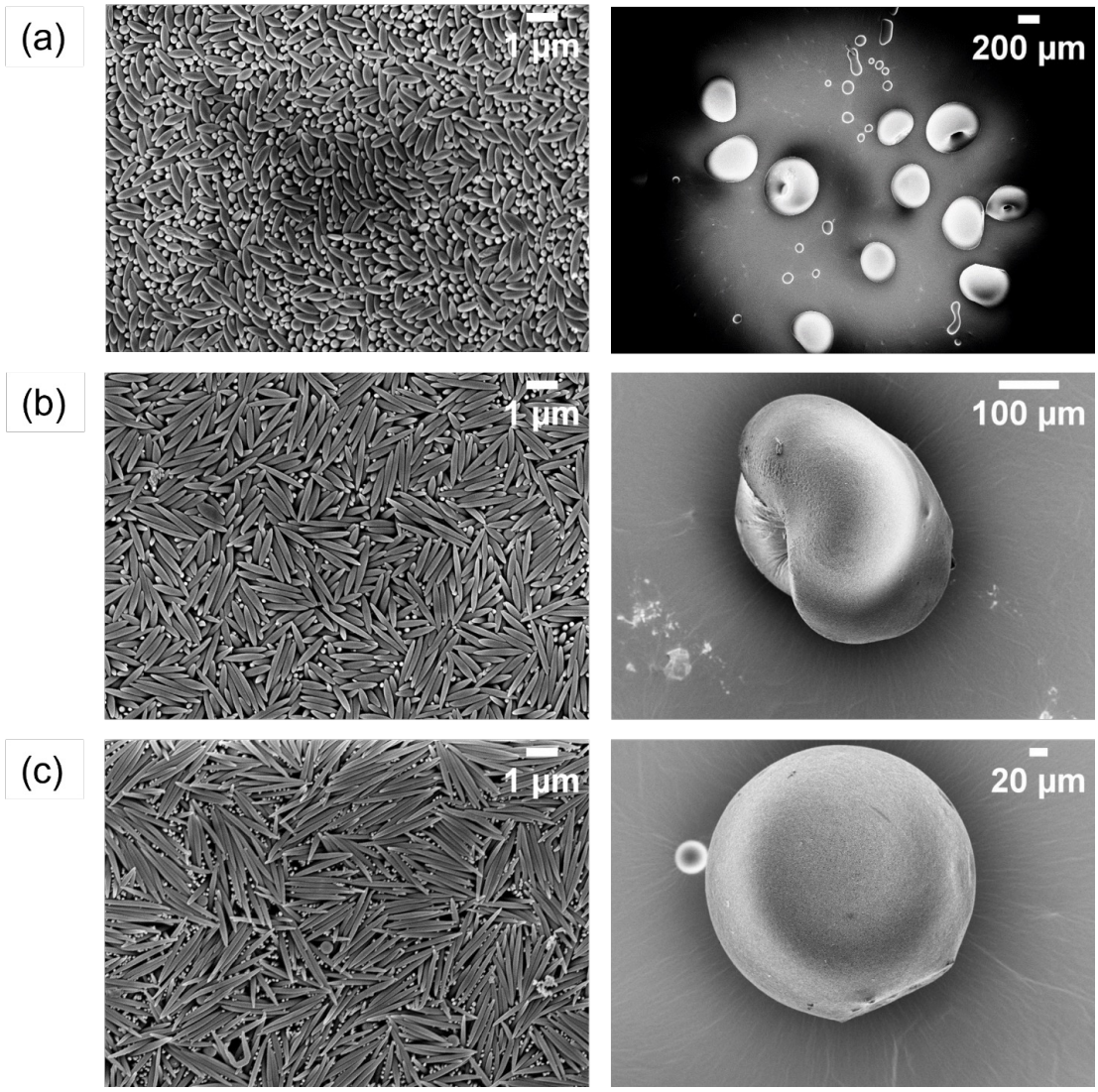

Fig. S5: SEM images of supraparticle surfaces, composed of ellipsoids of $\lambda =$ (a) 4, (b) 6, and (c) 11 at $170 \leq Pe_{\mathrm{e}} \leq 200$ (left column).The corresponding supraparticles showed buckling (right column).

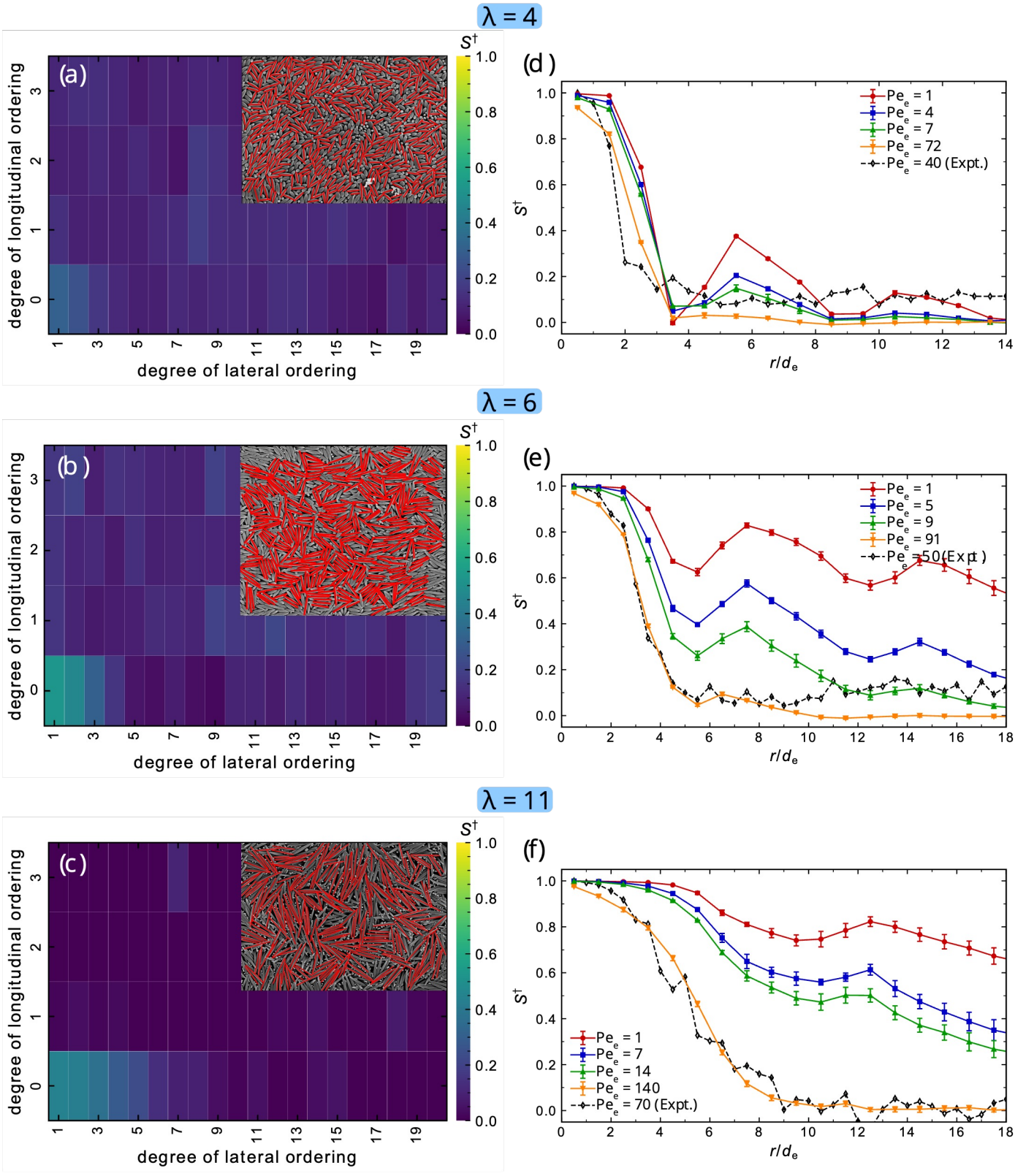

Fig. S6: (a-c) Orientational order parameter calculated from the surface SEM images. (d-f) show the Péclet number dependence of orientational order parameter.

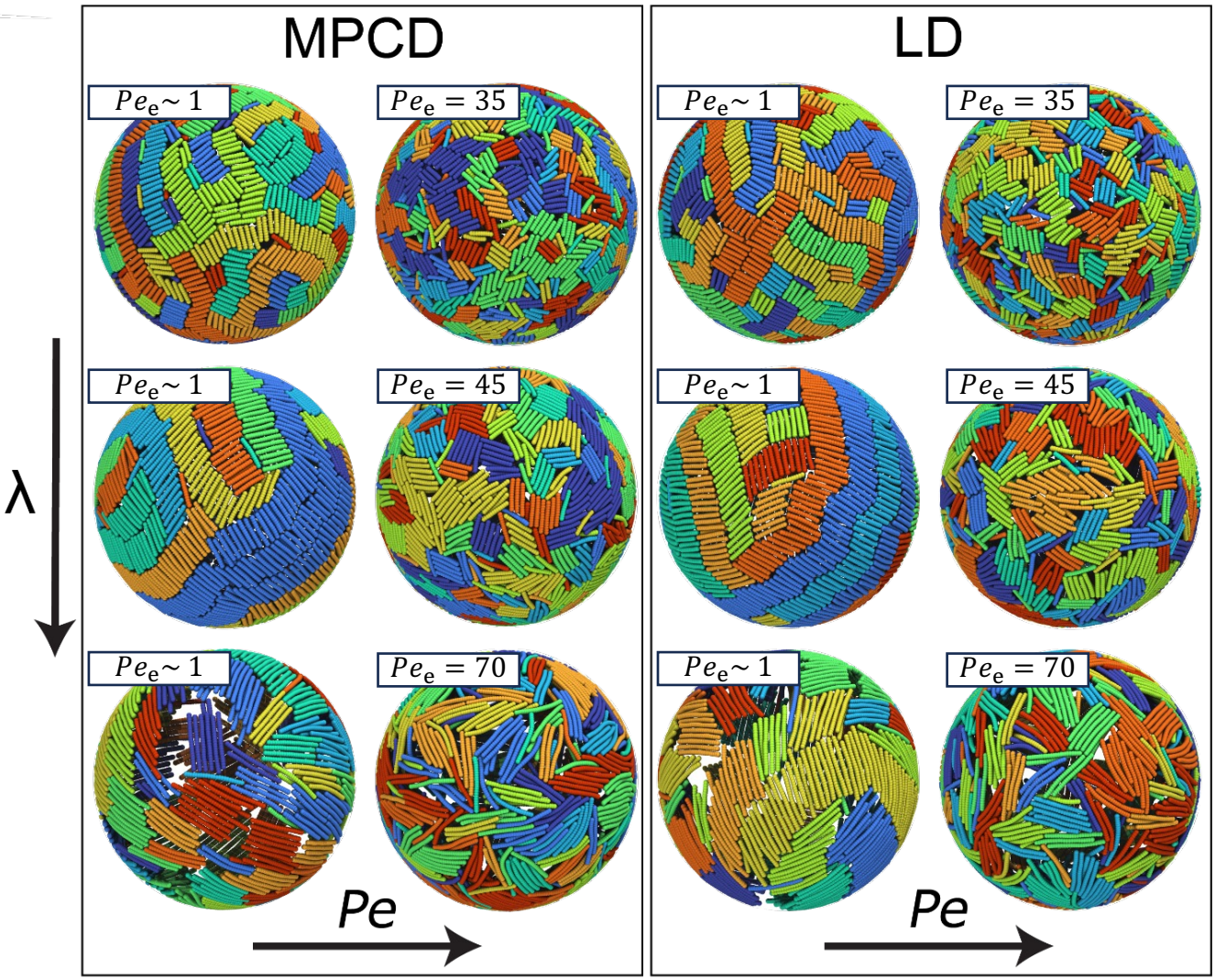

Fig. S7: Simulation snapshots showing the surface morphology of the supraparticles obtained from multi-particle collision dynamics (MPCD) and Langevin dynamics (LD) simulations for varying aspect ratios λ and Péclet numbers Pe.

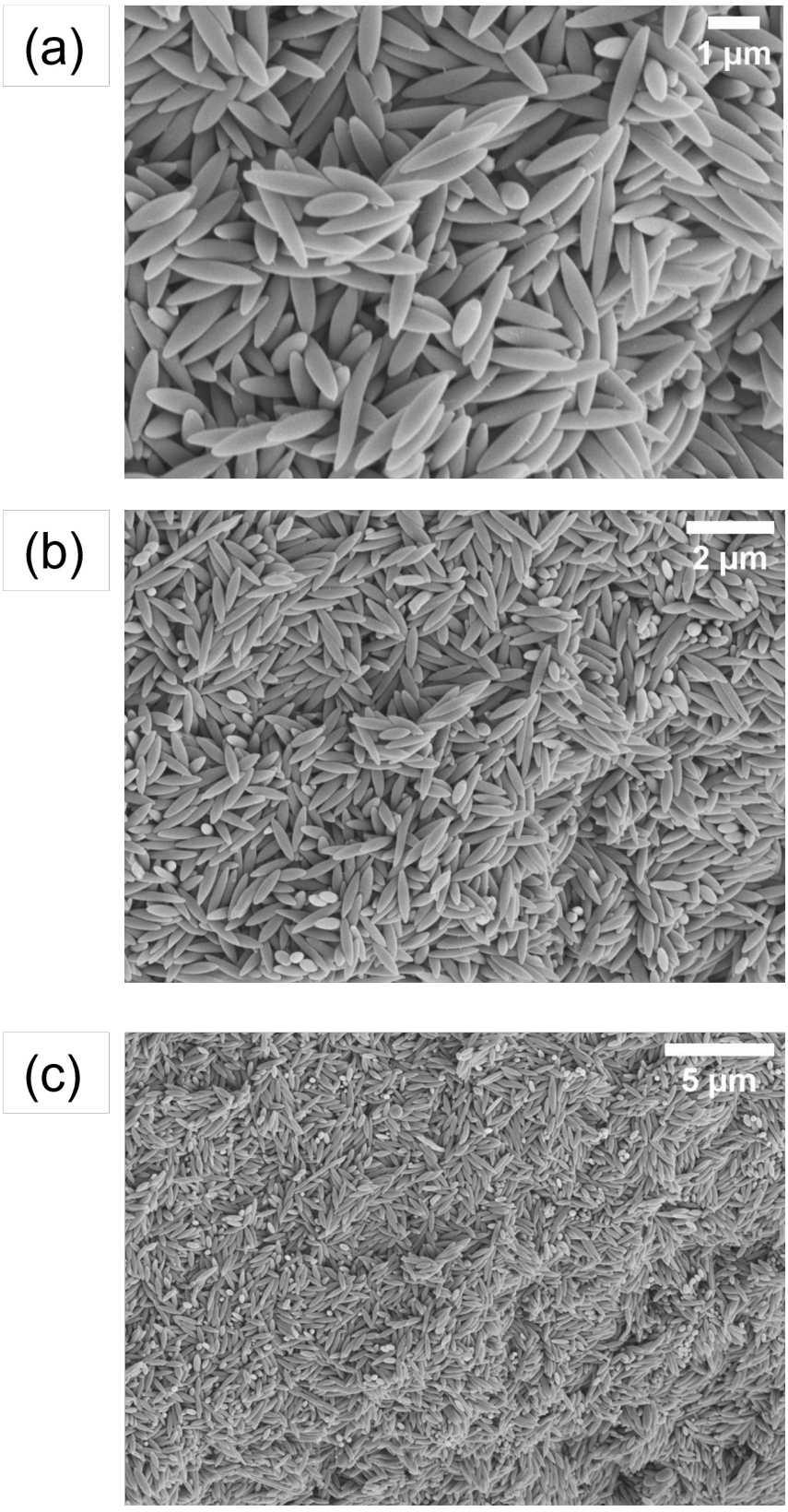

Fig. S8: The cross-section SEM images of supraparticles composed of $\lambda = 6$ ellipsoids at $Pe_e = 50$. Images were obtained by zooming out from the same region of interest (from (a-c)).

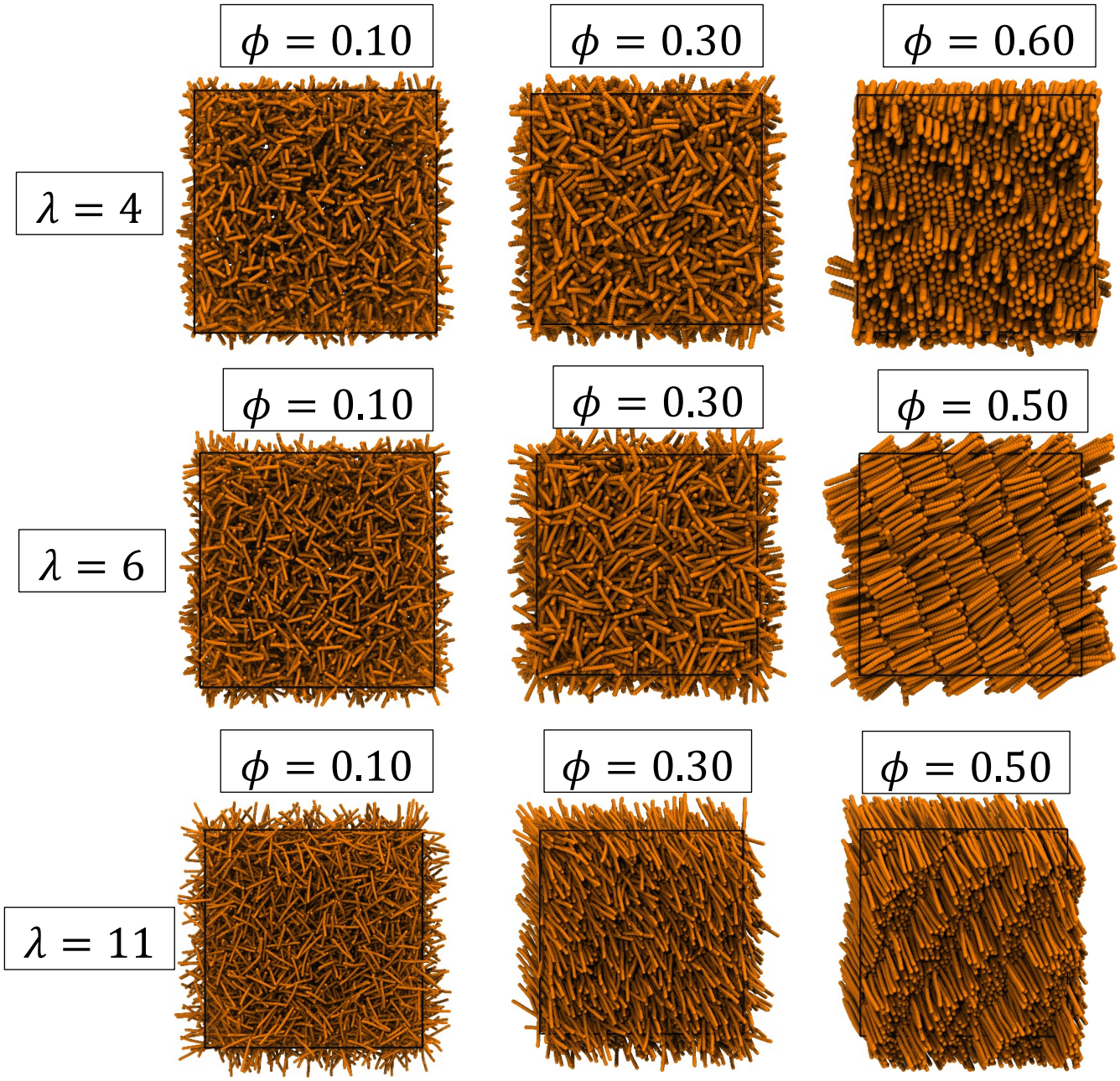

Fig. S9: Bulk simulations of pure-rod suspensions of varying aspect ratios (rows) and varying packing fractions (columns).

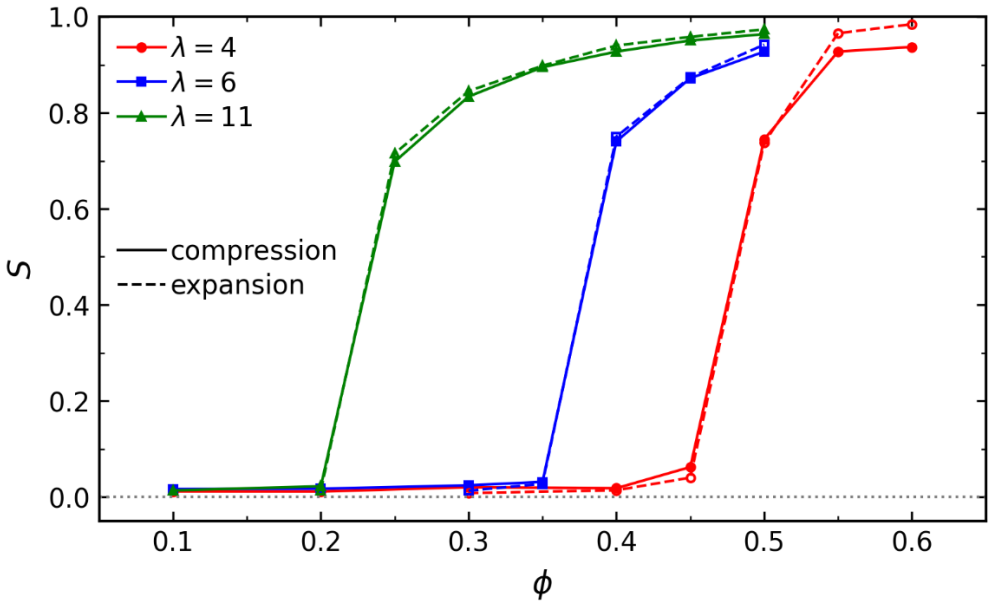

Fig. S10: Global order parameter obtained from bond order parameter in the bulk systems consisting of rods of varying aspect ratios.

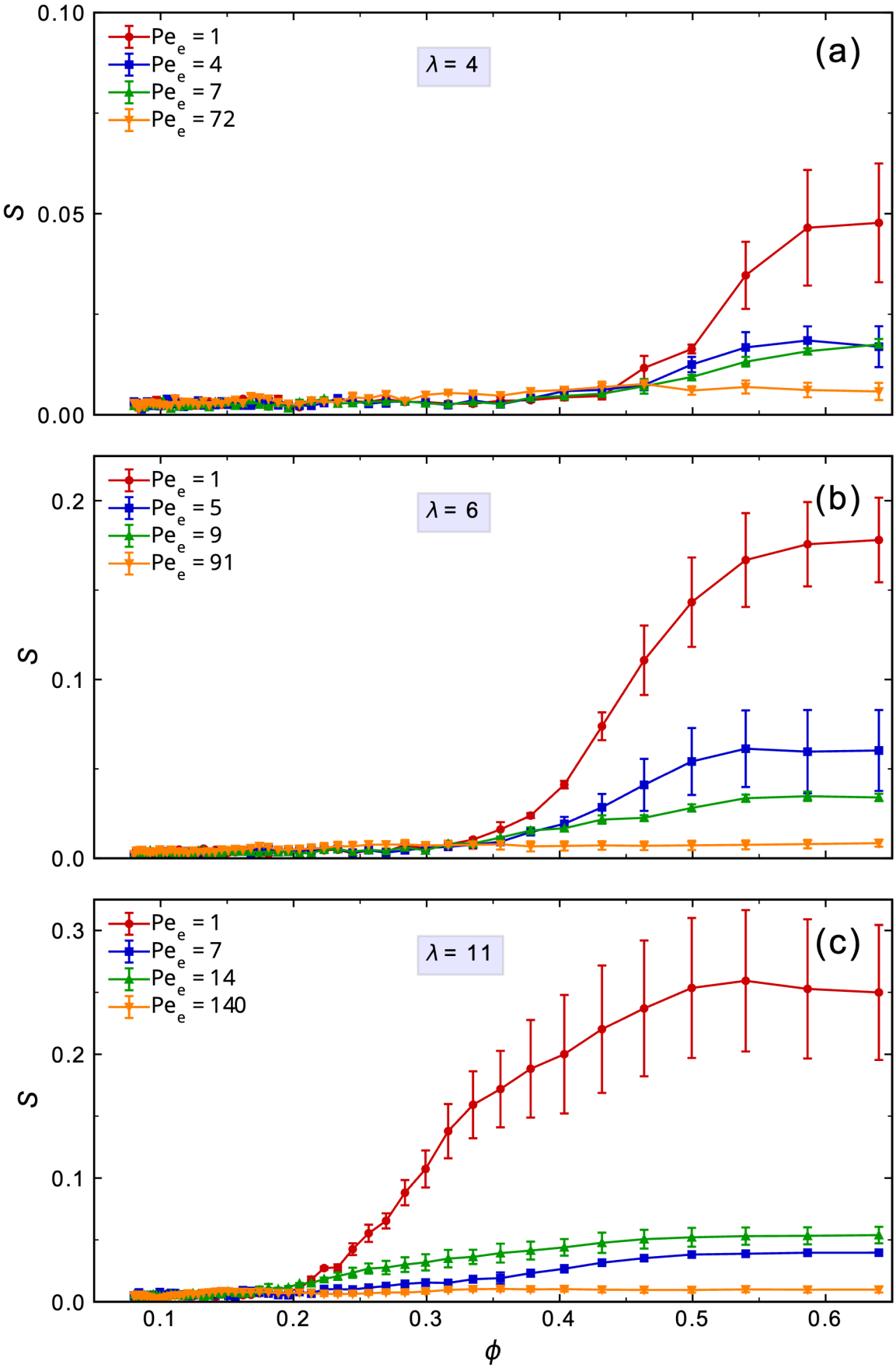

Fig. S11: Order parameter for drying droplet simulations with varying aspect ratios of rods, (a) 4, (b) 6, and (c) 11.

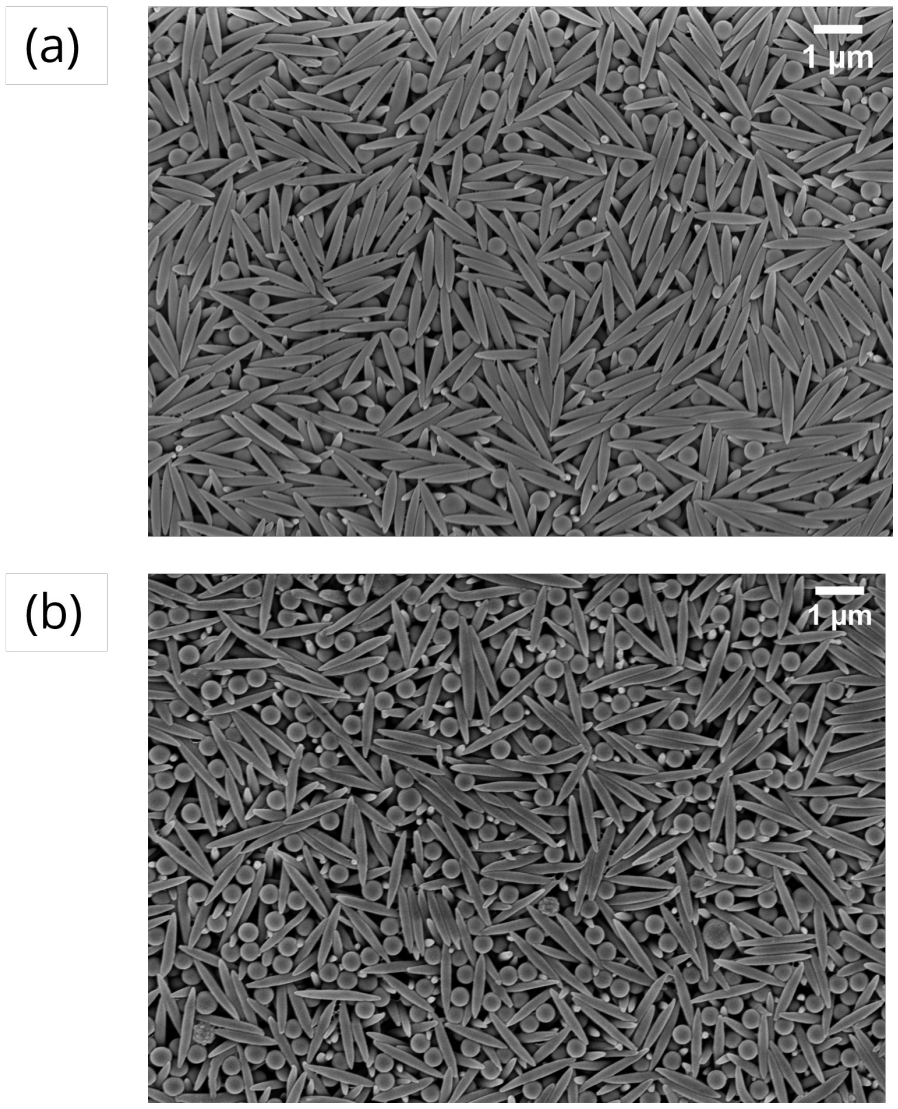

Fig. S12: SEM images showing the supraparticle surfaces composed of sphere-ellipsoid mixtures with ellipsoids of $\lambda = 6$ at (a) $\mathrm{Pe_e} = 50$ and $\mathrm{Pe_s} = 10$, (b) $\mathrm{Pe_e} = 120$ and $\mathrm{Pe_s} = 30$.

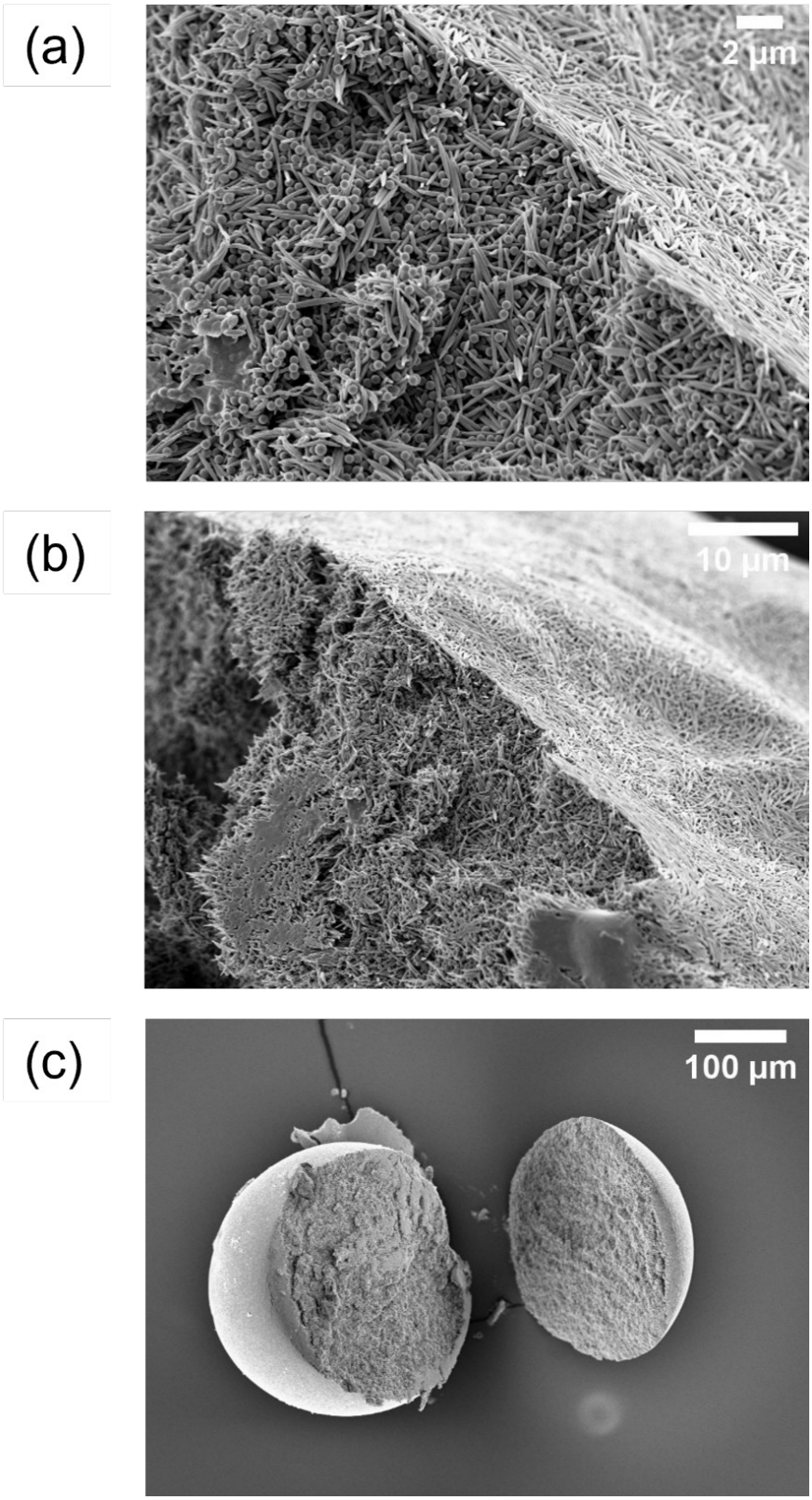

Fig. S13: The cross-section SEM images of supraparticles composed of sphere-ellipsoid mixtures with ellipsoids of $\lambda = 11$ at $Pe_{\mathrm{e}} = 50$ and $Pe_s = 10$. Images were obtained by zooming out from the same region of interest (from (a-c)). The cross-section images indicated a thin crust of ellipsoids on the surface followed by a random distribution of the ellipsoids and spheres inside the supraparticle.

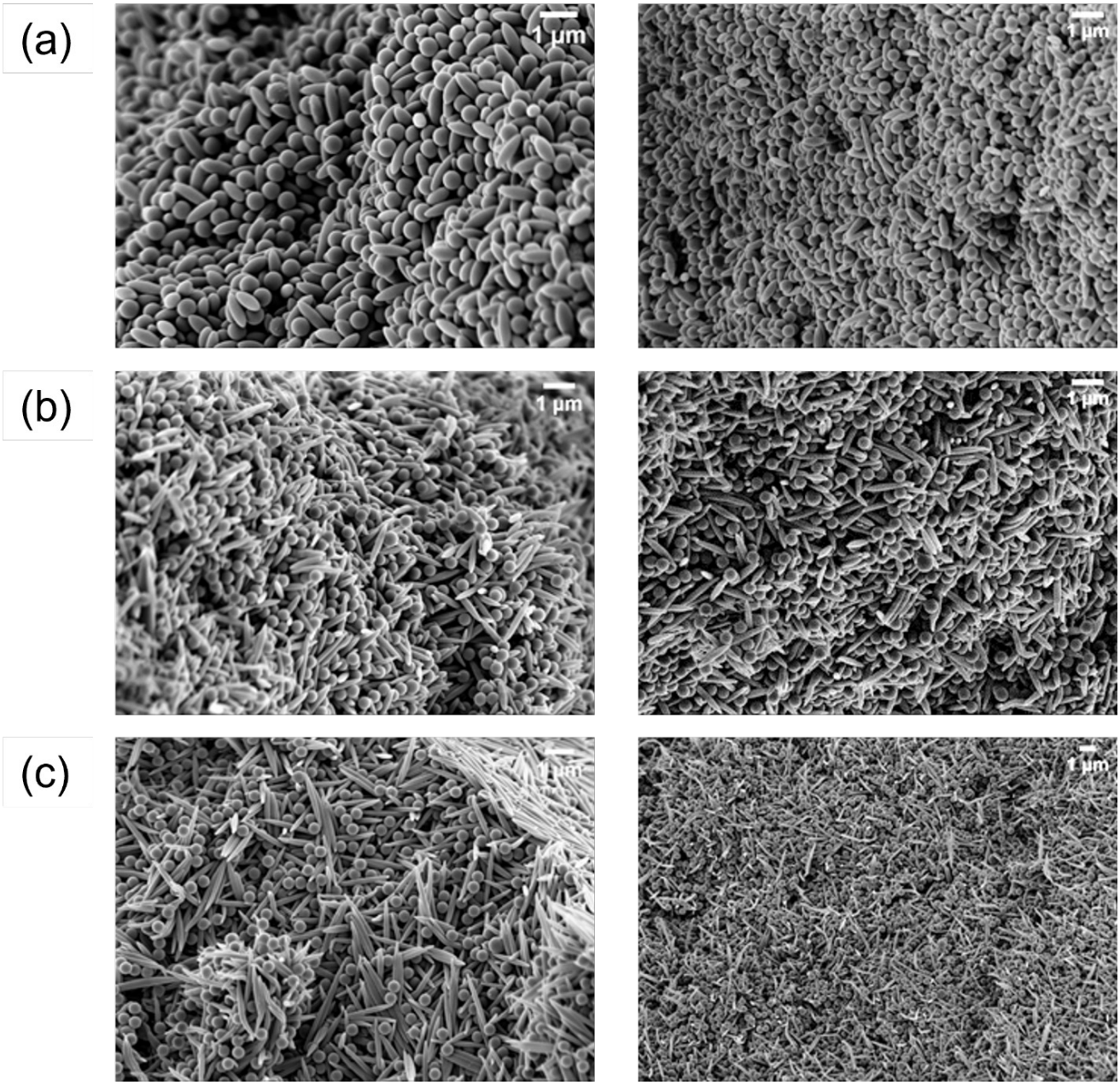

Fig. S14: The cross-section SEM images of supraparticles composed of sphere-ellipsoid mixtures with ellipsoids of λ = (a) 4, (b) 6, and (c) 11. The left column represents evaporation at $40 \leq Pe_{\mathrm{e}} \leq 50$ and $Pe_{\mathrm{s}} = 10$ and the right column represents evaporation at $130 \leq Pe_{\mathrm{e}} \leq 200$ and $30 \leq Pe_{\mathrm{s}} \leq 50$.

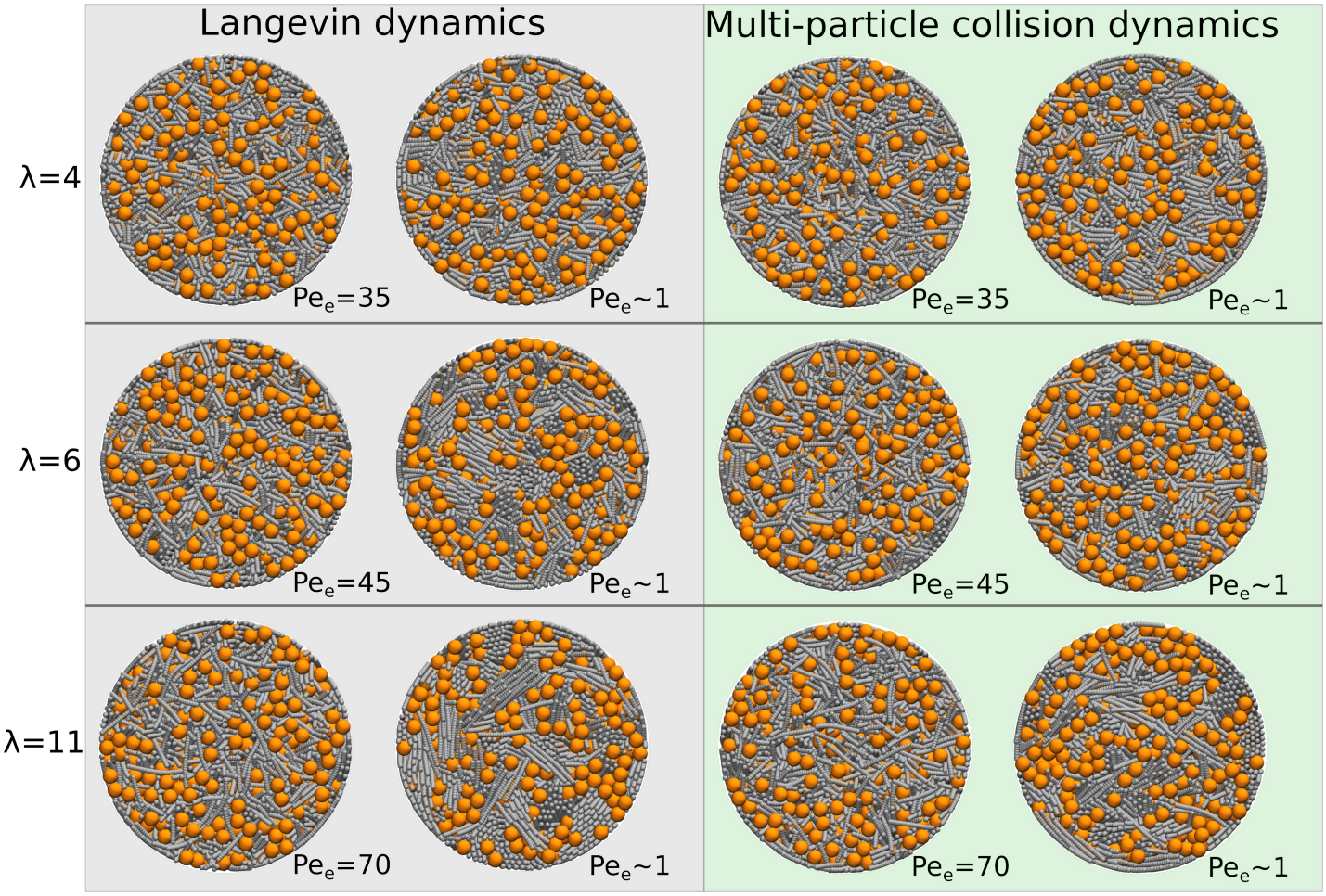

Fig. S15: Comparison of Langevin dynamics and multi-particle collision dynamics drying simulations.

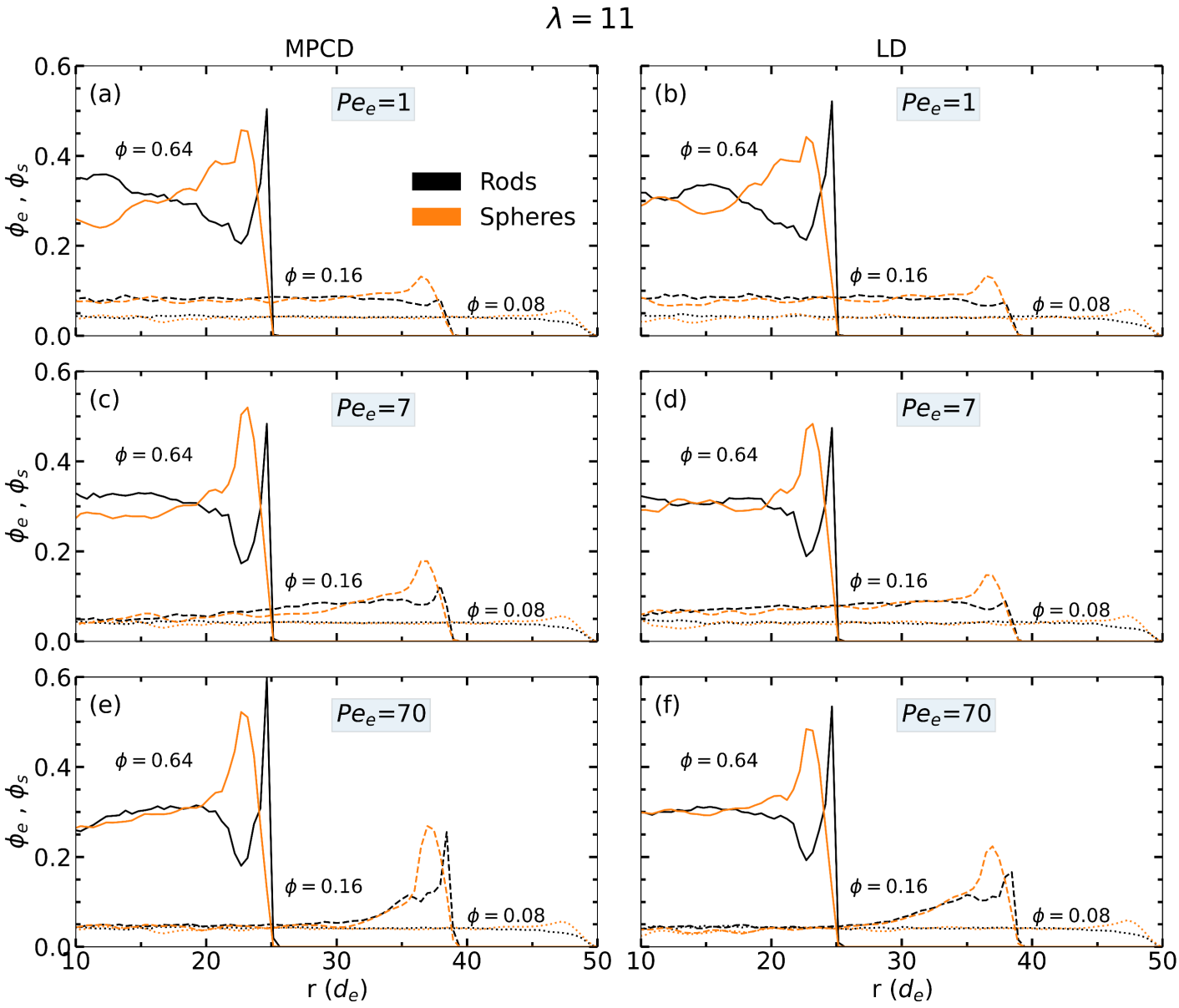

Fig. S16: Volume fraction profiles for rod ($\lambda = 11$) sphere mixture droplets with MPCD and LD methods.

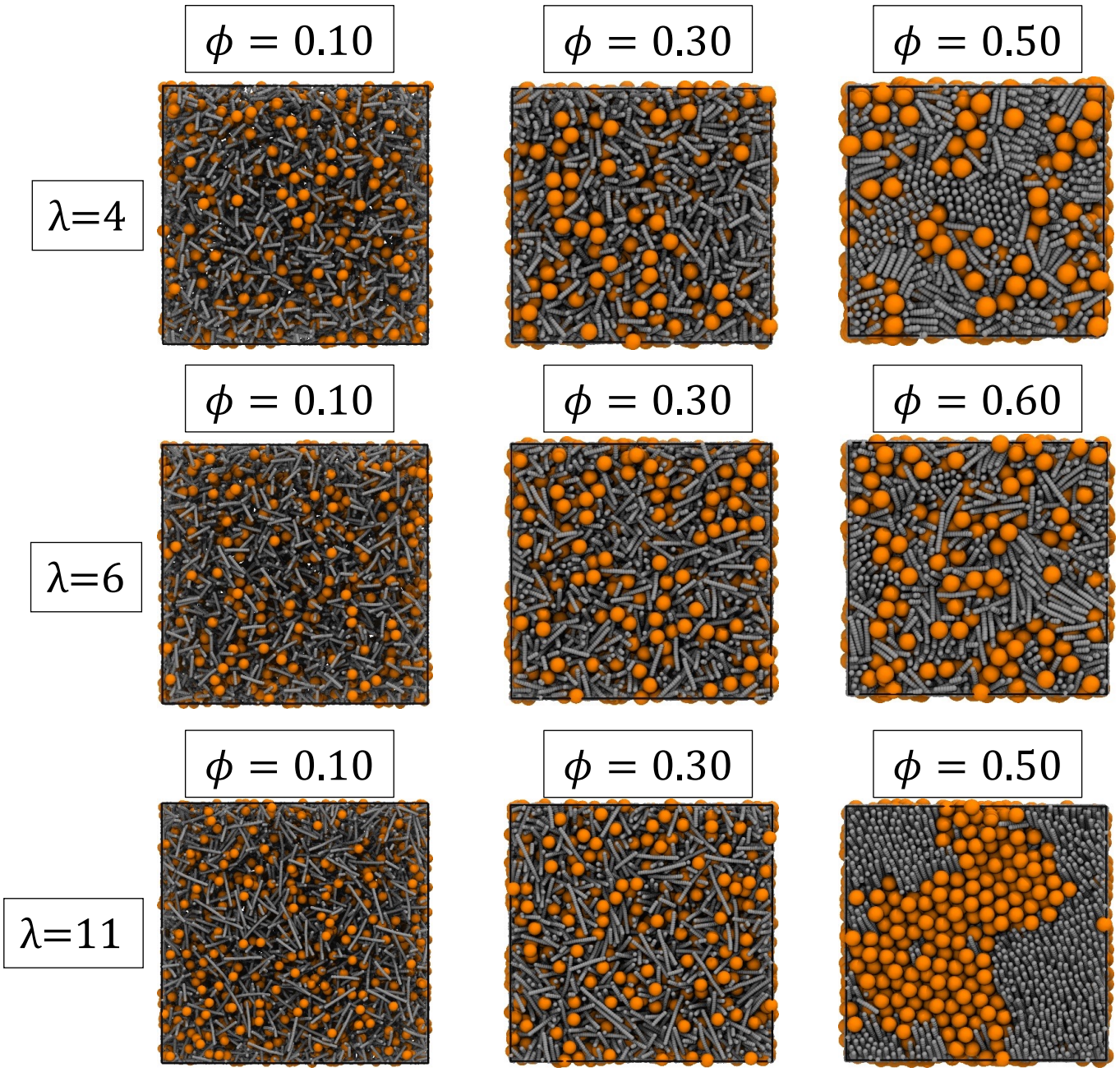

Fig. S17: Bulk simulations of sphere-rod mixtures of varying aspect ratios (rows) and varying packing fractions (columns).

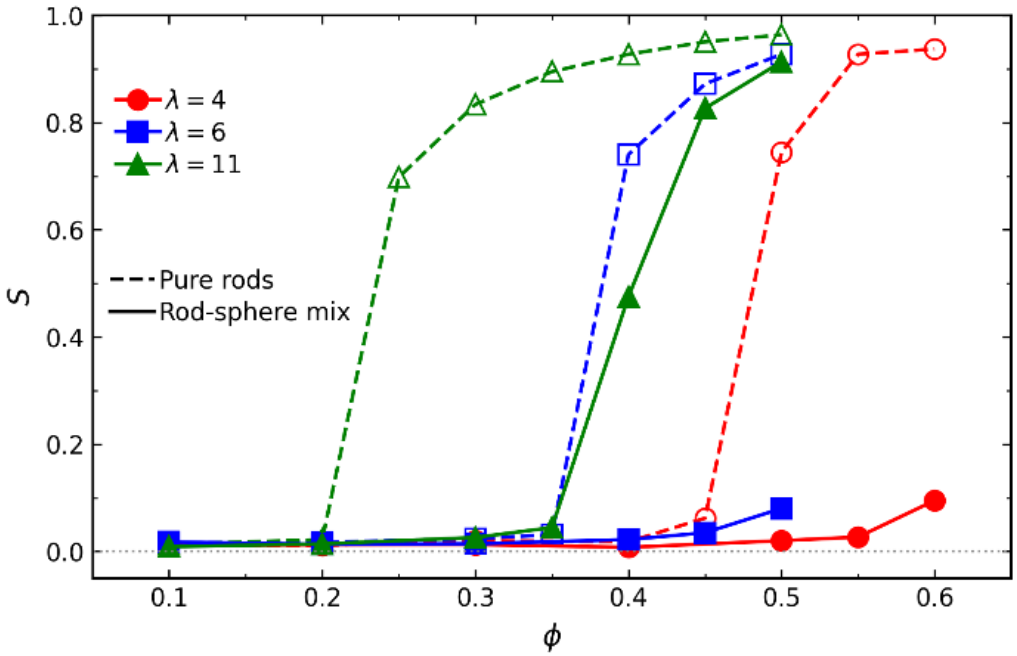

Figure S18: Global nematic ordering in bulk simulations of pure rods (dashed) and sphere-rod mixtures (solid)

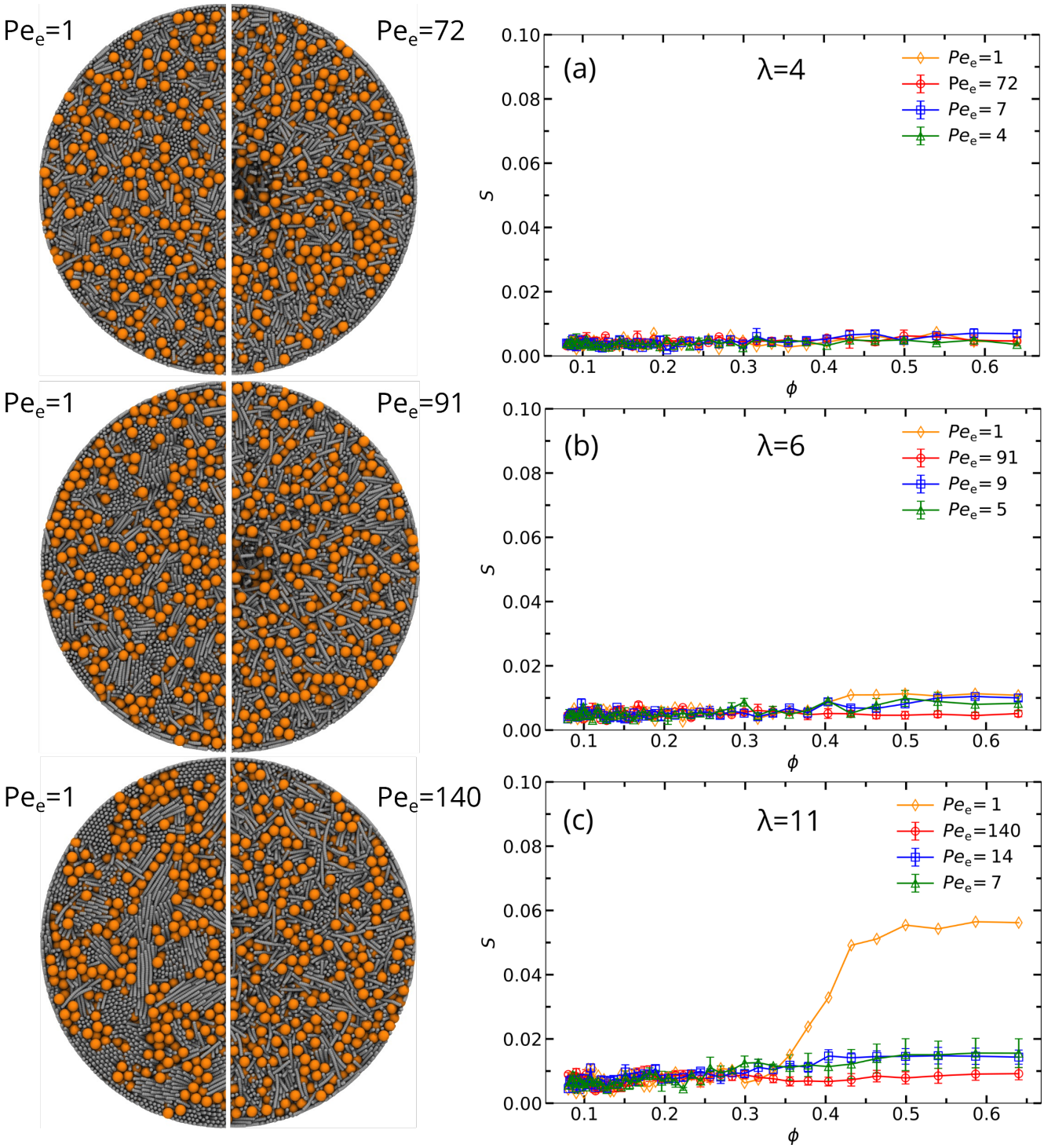

Figure S19: Global nematic ordering in droplets containing sphere-rod mixtures for (a) $\lambda = 4$, (b) $\lambda = 6$ and (c) $\lambda = 11$.